

Triggered star formation surrounding Wolf-Rayet star HD 211853

Tie Liu¹, Yuefang Wu¹, Huawei Zhang¹, Sheng-Li Qin²

Received _____; accepted _____

Accepted to ApJ

¹Department of Astronomy, Peking University, 100871, Beijing China; liutiepk@gmail.com

²I. Physikalisches Institut, Universität zu Köln, Zùlpicher Str. 77, 50937 Köln, Germany

ABSTRACT

The environment surrounding Wolf-Rayet star HD 211853 is studied in molecular emission, infrared emission, as well as radio and HI emission. The molecular ring consists of well-separated cores, which have a volume density of 10^3 cm^{-3} and kinematic temperature $\sim 20 \text{ K}$. Most of the cores are under gravitational collapse due to external pressure from the surrounding ionized gas. From SED modeling towards the young stellar objects (YSOs), sequential star formation is revealed on a large scale in space spreading from the Wolf-Rayet star to the molecular ring. A small scale sequential star formation is revealed towards core A, which harbors a very young star cluster. Triggered star formations is thus suggested. The presence of PDR, the fragmentation of the molecular ring, the collapse of the cores, the large scale sequential star formation indicate the "Collect and Collapse" process functions in this region. The star forming activities in core A seem to be affected by the "Radiation-Driven Implosion" (RDI) process.

Subject headings: Massive core:pre-main sequence-ISM: molecular-ISM: kinematics and dynamics-stars: formation

1. Introduction

The feedback of massive stars is expected to strongly influence on their surrounding interstellar medium (ISM) through the stellar radiation, energetic wind and ejection of elemental composition. The shock front emerging as the expansion of bubbles around massive stars can compress the ISM and trigger star formation in very dense layers (Chen et al. 2007).

Two models have been proposed to explain the effect of massive stars on star formation: Collect-and-Collapse (Elmegreen & Lada 1977) and Radiation-Driven Implosion (RDI) (Lefloch & Lazareff. 1994; Ogura 2010). The former one takes place in larger size in space (~ 10 pc) with longer timescale (a few Myr), whereas the later one in smaller size in space (~ 1 pc) with shorter timescale (0.5 Myr) (Ogura 2010). In the "Collect-and-Collapse" scenario, the ionization front generated from the HII region gathers molecular gases and collects a dense shell between the ionization front (IF) and shock front (SF). The gas and dust in the collected layer collapses to form stars when reaching the critical density (Chen et al. 2007; Ogura 2010). This process can self-propagate and lead to sequential star formation (Elmegreen & Lada 1977). Induced star formation through "collect and collapse" process has been revealed in the borders of several HII regions (Deharveng et al. 2003; Deharveng, Zavagno, & Caplan 2005; Zavagno et al. 2006, 2007; Deharveng et al. 2008; Pomarès, M. et al. 2009; Petriella et al. 2010; Brand et al. 2011). The so-called Radiation-Driven Implosion (RDI) process has been proposed to account for the evolution of bright-rimmed clouds whose surfaces are ionized by the UV photons from massive stars and triggered star formation therein (Bertoldi 1989; Bertoldi & McKee 1990; Hester & Desch 2005; Miao et al. 2009; Gritschneider et al. 2009; Bisbas et al. 2011; Haworth & Harries. 2012). The ionization fronts generate a shock compressing into the cloud to cause the dense clumps to collapse (Chen et al. 2007). Candidates for star formation by RDI have been found in many bright rimmed clouds associated with IRAS point sources (Sugitani et al. 1991; Sugitani & Ogura 1994; Urquhart et al. 2004, 2006, 2007; Morgan et al. 2010).

The Wolf-Rayet stars initially more massive than $\sim 40 M_{\odot}$, have typical mass loss rates of $10^{-5} M_{\odot} \text{ yr}^{-1}$ and strong stellar winds faster than 1000 km s^{-1} . They can blow stellar wind bubbles having radius of ~ 10 to $\sim 100 \text{ pc}$ and expanding velocities of several km s^{-1} (Marston 1996; Martín-Pintado et al. 1999). The expanding bubbles can push away the molecular gas and create molecular layers which fragment into condensations well separated in due time. The ”collect-and-collapse” process is expected to happen in the shells swept up by such expanding stellar wind bubbles (Whitworth et al. 1994). However, the samples of triggered star formation surrounding Wolf-Rayet stars are rare and seldom previous works focus on the star forming activities in such regions. In this paper, we provide such a sample region where triggered star formation is witnessed.

HD 211853 locates at the center of an optically bright region named as shell B in the HII region Sh2-132 (Sharpless 1959; Harten, Felli & Tofani. 1978). The HII region linked to shell B is excited by a massive O-type star BD+55°2722 and the WR star HD 211853 (Vasquez et al. 2010). While HD 211853 is the main ionizing source of the ring nebula (Cappa et al. 2008). The Wolf-Rayet star HD 211853 (WR 153ab) is a binary system. The spectral type of the two WR components are WN6 and WCE+06 (Nishimaki et al. 2008). The velocity of its stellar wind is as high as $1500\text{-}1800 \text{ km s}^{-1}$, leading to a high mass-loss rate of $10^{-4.5} M_{\odot} \text{ yr}^{-1}$ (Nishimaki et al. 2008). A ring nebular associated with HD 211853 is easily identified in radio emission and PAH emission, as well as molecular emission (Vasquez et al. 2010; Cappa et al. 2008). Fig.1 presents a composite color image of this region. Blue corresponds to the DSS-R optical emission, green to the radio emission detected in the Canadian Galactic Plane Survey (CGPS, Taylor et al. (2003)) at 1420 MHz , and red to $8.3 \mu\text{m}$ emission detected at MSX A band.

It can be seen that the radio emission is embraced by the $8.3 \mu\text{m}$ emission, which forms a ring-like structure. A photodissociated region (PDR) has been identified and possible triggered star formation in this region is suggested (Vasquez et al. 2010). As shown in Figure 2 of

Saurin et al. (2010), three star clusters "Teutsch 127", "SBB 1" and "SBB 2" have been found in this region, and the hierarchical structure and the age distribution of the star clusters show evidence of triggered star formation (Saurin et al. 2010). However, the studies of the star forming activities in this region are far from mature. In this paper, through detailed analysis of molecular emission and characters of young stellar objects (YSOs), we have revealed the picture of triggered star formation in this region.

2. Observations and Database

The observations of ^{12}CO (1-0), ^{13}CO (1-0) and C^{18}O (1-0) were carried out with the Purple Mountain Observatory (PMO) 13.7 m radio telescope in 2011 January. The new 9-beam array receiver system in single-sideband (SSB) mode was used as front end. The array pixels are sideband separation SIS mixers yielding 18 independent IF outputs. The properties of the SIS mixers are introduced in Shan et al. (2009). ^{12}CO (1-0) was observed at upper sideband, while ^{13}CO (1-0) and C^{18}O (1-0) were observed simultaneously at lower sideband. FFTS spectrometers were used as back ends, which have a total bandwidth of 1 GHz and 16384 channels, corresponding to a velocity resolution of 0.16 km s^{-1} for ^{12}CO (1-0) and 0.17 km s^{-1} for ^{13}CO (1-0) and C^{18}O (1-0). The half-power beam width (HPBW) is $56''$ and the main beam efficiency is ~ 0.5 during our observation period. The pointing accuracy of the telescope was better than $4''$. The typical system temperature (T_{sys}) in SSB mode is around 110 K and varies about 10% for each beam. The On-The-Fly (OTF) observing mode was applied. The antenna continuously scanned a region of $22' \times 22'$ centered on the Wolf-Rayet star HD 211853 with a scan speed of $20'' \text{ s}^{-1}$. The OTF data were then converted to 3-D cube data with a grid spacing of $30''$. Because the edges of the OTF maps are very noisy, only the central $14' \times 14'$ region is selected to be analyzed. The typical rms noise level was 0.2 K in T_{A}^* for ^{12}CO (1-0), and 0.1 K for ^{13}CO (1-0) and C^{18}O (1-0). For the data analysis, the GILDAS software package including

CLASS and GREG was employed (Guilloteau & Lucas 2000).

Neutral hydrogen (HI) 21 cm line data were from CGPS with intensities shown as brightness temperature T_{mb} . The synthesized beam and rms bright temperature in a 0.82 km s^{-1} channel are $\sim 1'$ and 3 K, respectively. Radio continuum data and images at 1420 MHz were extracted from the CGPS (Taylor et al. 2003) and the NRAO VLA Sky Survey (NVSS, Condon et al. (1998)). The positions and fluxes of the NVSS sources are obtained from the NVSS catalog (Condon et al. 1998). The CGPS 1420 MHz data have a synthesized beam of $\sim 50''$ and a noise level of $\sim 3 \text{ mJy beam}^{-1}$. The NVSS image has a spatial resolution of $45''$ and the rms brightness fluctuation of $\sim 0.45 \text{ mJy beam}^{-1}$ (Stoke I). MSX A-band data were extracted from the MSX Galactic Plane Survey (Price et al. 2001), which has a spatial resolution of $\sim 18''.3$. Spitzer IRAC data and 2MASS data were obtained from Qiu et al. (2008), both of which have good spatial resolutions of $\sim 2''$. We also obtained SCUBA $450 \mu\text{m}$ and $850 \mu\text{m}$ continuum data from the SCUBA Legacy Catalogues (Di Francesco et al. 2008). At $850 \mu\text{m}$ and $450 \mu\text{m}$, the resolutions of SCUBA data are of $\sim 14''$ and $\sim 9''$, respectively.

3. Results

3.1. Molecular emission

The ^{12}CO (1-0), ^{13}CO (1-0) and C^{18}O (1-0) emissions were observed simultaneously. However we didn't detected any C^{18}O (1-0) emission in this region above 3σ (0.3 K), indicating low column density in this region. ^{12}CO (1-0) emission was detected in almost the whole region even at the position of the Wolf-Rayet star HD 211853. ^{13}CO (1-0) emission was only detected in the ring-like region, but not within it. The detailed analysis of the molecular emission are below.

3.1.1. *The systemic velocity of the molecular clumps*

In Fig.2, we present the 1' averaged spectrum of ^{12}CO (1-0) at the position of the Wolf-Rayet star. ^{12}CO (1-0) emission is significantly detected. From gaussian fit, the peak antenna temperature is 0.38 ± 0.02 K, about 8σ level (1σ equals to 0.05 K estimated from the baseline). It has a line width of 4.1 ± 0.2 km s $^{-1}$ and a peak velocity of -43.4 ± 0.01 km s $^{-1}$.

The left panel of Fig.3 presents the $14' \times 14'$ averaged spectra of HI 21 cm line, ^{12}CO (1-0) line and ^{13}CO (1-0) line. The right panel of Figure 3 shows the zoomed in averaged spectra of ^{12}CO (1-0) line and ^{13}CO (1-0). There are two components in the ^{12}CO (1-0) and ^{13}CO (1-0) emission, which is also noticed by Vasquez et al. (2010). The narrow one peaks at -50 km s $^{-1}$, while the other broader one ranges from -48 km s $^{-1}$ to -39 km s $^{-1}$.

Are both the components related to this region? We argue that the -50 km s $^{-1}$ maybe a foreground cold cloud, not part of this region based on two aspects.

(1). The integrated emission of ^{12}CO (1-0) in the first two panels of Figure 5 is concentrated in an isolated and compact core (denoted as core "I") at north-west of HD 211853. We didn't detected this component in the other positions. Additionally, from the P-V diagrams in Fig.6, one can see the -50 km s $^{-1}$ component is also not connected to the other component in velocity space. Vasquez et al. (2010) argued the ^{12}CO (1-0) emission between -53.4 and -46.0 km s $^{-1}$ is also associated with the ring nebular. However, their conclusion may be misleading because their integrated map is contaminated by the emission between -48 to -46 km s $^{-1}$. As the channel map shows, the emission in their cloud E and F is dominated by the emission between -48 and -39 km s $^{-1}$, rather than -50 km s $^{-1}$ component.

(2). The left panel of Figure 4 presents the spectra of HI 21 cm line, ^{12}CO (1-0) line and ^{13}CO (1-0) line at the peak of core "I". The right panel of Figure 4 shows the zoomed in spectra of ^{12}CO (1-0) line and ^{13}CO (1-0). One can see the HI emission at the peak of core "I" has a very

narrow absorption dip. Together with the narrow line width of the molecular emission, an HI Narrow Self-Absorption (HINSA) system can be identified, suggesting core "I" more likely be a foreground cold cloud (Li & Goldsmith 2003). As shown in Table 2, the kinematic temperature of core "I" (14.6 ± 0.3 K) is much lower than that of core "F" (21.7 ± 1.0 K), indicating that core "I" is more quiescent than core "F".

In conclusion, the -50 km s^{-1} molecular component is more likely from a foreground cold cloud, rather than being a part of the molecular environment surrounding HD 211853. But because the -50 km s^{-1} molecular component is very near from the ring nebular in spatial and velocity space, it may be also interact with the expanding molecular ring, which needs further observations to confirm.

From the gaussian fit, the averaged ^{13}CO (1-0) spectrum peaks at $-43.6 \pm 0.1 \text{ km s}^{-1}$, very similar to that of the ^{12}CO (1-0) emission taken from the central Wolf-Rayet star ($-43.4 \pm 0.01 \text{ km s}^{-1}$). Thus we adopt -43.5 km s^{-1} as the overall systemic velocity of the molecular emissions in this region.

3.1.2. *The properties of molecular cores*

Fig.5 displays the channel maps of ^{12}CO (1-0) emission in contours overlaid on the $8.3 \mu\text{m}$ emission in MSX A band. The middle velocities of each panel are plotted on the upper-right corners. In each panel, the integrated velocity interval is 2 km s^{-1} . The contours are from 20% to 90% of the peak intensity in each panel. It can be seen that the ^{12}CO (1-0) emission is very clumpy. The blue-shifted gas (-46 km s^{-1} panel) distributes in the western and southern region, while the red-shifted gas (-40 km s^{-1} panel) mainly in the northern and eastern region, indicating a velocity gradient through north-east to south-west. The gas at -42 and -44 km s^{-1} forms a ring-like structure harboring several well separated cores. The ring-like molecular structure perfectly

coincides with the $8.3 \mu\text{m}$ emission in MSX A band.

Fig.6 presents the P-V cuts along two orientations denoted by the red dashed lines in Fig.7. From the P-V diagrams, it's clearly to see that the -50 km s^{-1} component is separated with the -43.5 km s^{-1} component. An amazing aspect from the P-V cuts is that the relative velocity of the gas increases with the distance to the WR star from near to far, following a "Hubble law" like distribution, as denoted by the dashed lines.

Fig.7 displays the integrated intensity map of ^{13}CO (1-0) overlaid on the $8.3 \mu\text{m}$ emission in grey scale, which is integrated from -48 to -39 km s^{-1} . The contours are from 10% ($\sim 8\sigma$) to 90% of the peak emission. Eight cores are identified and denoted from "A" to "H". The Wolf-Rayet star HD 211853 is drawn as "cross". IRAS, MSX and AKARI point sources are marked with "boxes", "Triangles" and "stars", respectively. However, one should keep in mind that many of these point sources may be not real, but just correspond to some variations of brightness in the infrared emission along the filamentary structures. More observations are needed to constraint their properties. But, for convenience, we still call them "point sources" in the following text. These cores form a ring-like structure surrounding HD 211853, and are associated with the $8.3 \mu\text{m}$ emission in MSX A band. Most of the infrared point sources distribute in the molecular ring. Core "A" is associated with an IRAS source "IRAS 22172+5549", while the emission peaks of the other cores seem to be separated from the infrared point sources, which will be discussed later in section 4.3.

Taking into account of the effect of beam smearing, the radii of the cores are calculated as $R = \frac{\sqrt{4A/\pi - \theta_b^2}}{2}$, where A is the projected area of each core and θ_b is the beam width. Adopting a distance of 3 kpc (Cappa et al. 2008), the radii of the cores are calculated and listed in the fourth column of Table 1. The average radius is 1 pc.

Fig.8 presents the spectra of ^{12}CO (1-0), ^{13}CO (1-0) and C^{18}O (1-0) at the emission peaks of the cores. The spectra at core "E" is totally blue-shifted, while core "H" red-shifted. The peak

velocities of the other cores coincide with or slightly deviate from the systemic velocity. The results of gaussian fit to these spectra are listed in Table 1. Core "G" has the largest line width and antenna temperatures, while core "H" has the smallest ones. The line width of ^{13}CO (1-0) ranges from 1.3 to 2.6 km s^{-1} with a mean value of 2.1 km s^{-1} .

Assuming ^{12}CO (1-0) emission is optically thick and ^{13}CO (1-0) optically thin, we derived the parameters of the cores including the excited temperatures T_{ex} , column densities of H_2 , N_{H_2} , and optical depth of ^{13}CO (1-0) lines under local thermal equilibrium (LTE) assumption following Garden et al. (1991). Typical abundance ratios $[\text{H}_2]/[^{12}\text{CO}]=10^4$ and $[^{12}\text{CO}]/[^{13}\text{CO}]=60$ were used in calculations (Deharveng et al. 2008). The volume density of H_2 is calculated as $n_{\text{H}_2}=N_{\text{H}_2}/2R$. Then the core mass can be derived as $M=\frac{4}{3}\pi \cdot R^3 \cdot n_{\text{H}_2} \cdot m_{\text{H}_2} \cdot \mu_g$, where m_{H_2} is the mass of a hydrogen molecule and $\mu_g=1.36$ is the mean atomic weight of the gas. The derived parameters are listed from column 3 to 7 in Table 2. The N_{H_2} ranges from 1.8×10^{21} to $1.4 \times 10^{22} \text{ cm}^{-2}$. The optical depth of ^{13}CO (1-0) is around 0.3. The core masses range from 21 M_\odot ("H") to 1061 M_\odot ("G") with a mean value of 400 M_\odot .

We also applied RADEX (Van der Tak et al. 2007), a one-dimensional non-LTE radiative transfer code, which uses the escape probability formulation assuming an isothermal and homogeneous medium without large-scale velocity fields, to constraint on physical conditions of the cores, such as density and kinetic temperature. In the first running, we explore a range of H_2 volume densities and temperatures of $[10^2, 10^6] \text{ cm}^{-3}$ and $[5, 50] \text{ K}$. The molecular column densities, which are also input parameters required, are fixed according to the H_2 volume densities as $N(\text{X})=n_{\text{H}_2} \cdot 2R \cdot X(x)$, where $X(x)$ is the relative abundance ratio of the molecule. For ^{12}CO (1-0), $X(x)=10^{-4}$, and for ^{13}CO (1-0), $X(x)$ is adopted as 1.67×10^{-6} . The model parameters were picked out if satisfying $|T_{mod} - T_{obs}| \leq 3\sigma$, where T_{mod} and T_{obs} are the modeled and observed brightness temperature of the molecule transition, respectively. As shown in the left panel of Fig.9, the kinematic temperatures and H_2 volume densities can be well constrained by modeling

both ^{12}CO (1-0) and ^{13}CO (1-0) lines. Two geometries, static spherical and expanding spherical (similar to large velocity gradient (LVG) approximation), were chosen in this running. It can be seen that both geometry assumptions give nearly the same results for ^{13}CO (1-0) lines, while for ^{12}CO (1-0) lines, static spherical models give slightly higher volume densities than expanding spherical at higher kinematic temperatures. However, in the overlapping region, the deviations of the two geometries are small enough to be ignored. We narrowed the parameter space in the second running assuming the expanding spherical geometry. The range of H_2 volume densities and temperatures in the second running are of $[2.5 \times 10^2, 10^4] \text{ cm}^{-3}$ and $[8, 30] \text{ K}$, respectively. As shown in the right panel of Fig.9, the kinematic temperatures and volume densities of H_2 can be well constrained in the overlapping region of ^{12}CO (1-0) and ^{13}CO (1-0) tracks. The best physical parameters from RADEX are obtained by averaging the parameters in the overlapping region, and displayed from column 7 to 14 in Table 2.

It's interesting to notice that the excitation temperatures of ^{12}CO (1-0) obtained from RADEX are perfectly consistent with that calculated under LTE assumption. The excitation temperatures of ^{13}CO (1-0) are much lower than that of ^{12}CO (1-0). The optical depths of ^{13}CO (1-0) obtained from RADEX are larger than that obtained from LTE conditions. The kinematic temperatures are always larger than the excitation temperatures of ^{12}CO (1-0). The volume densities of H_2 and core masses calculated in RADEX roughly agree with that from LTE calculations.

3.2. Radio continuum emission, HI emission and PAH emission

From the radio emission detected in CGPS at 1420 GHz, Vasquez et al. (2010) obtained an rms $n_e = 20 \text{ cm}^{-3}$ and $M_{\text{HII}} = 1500 M_{\odot}$ in this region. As shown in the upper panels of Fig.10, nine NVSS radio sources (shown in blue dashed contours) locate in this region, and most of them are bordered by the $8.3 \mu\text{m}$ emission ring shown in red solid contours. The nine radio sources are not individual HII regions, but high brightness components of the large HII region. They reflect the

fluctuation and non-uniformity of the ionized gas distribution within the large HII region. The Wolf-Rayet star is associated with NVSS source "1", and the molecular core "A" is associated with NVSS source "5". Following Panagia & Walmsley (1978), the electron densities, emission measures and masses of ionized hydrogen of these NVSS sources are derived by assuming an electronic temperature of 8000 K. However, those parameters listed in Table 3 can only be treated as a lower limit due to the missing flux of VLA. NVSS "4", "5" and "2" in the yellow dashed box show very high electronic densities and form an ionization front interacting with the molecular ring. NVSS "1" and "3" seem to interact with the northern part of the molecular ring, mainly with core "G".

We integrated HI emission from -48 km s^{-1} to -39 km s^{-1} and displayed the integrated intensity map in grey scale in the upper panel of Fig.10. The HI emission is very diffuse with a integrated intensity gradient in the N-S orientation. The HI emission also has a shell-like appearance in the southern part, which is associated with the $8.3 \mu\text{m}$ emission. An HI cavity is found within the yellow dashed box, where the ionization front exists. Assuming that the HI 21 cm line is optically thin and spin temperature $T_s \gg h\nu/k$, the average column density of HI can be calculated as $N_{HI} = 1.82 \times 10^{18} \times \int \overline{T_b} dv \text{ (cm}^{-2}\text{)}$. Based on the averaged spectrum of HI shown in the left panel of Fig.3, the average column density of HI in the whole region of shell B is about $9.4 \times 10^{20} \text{ cm}^{-2}$. The total mass of HI is estimated to be $1100 M_\odot$, which is comparable to the total mass of HII ($\sim 1500 M_\odot$) (Vasquez et al. 2010).

The ring-like feature of the $8.3 \mu\text{m}$ emission in MSX A band has been revealed by Cappa et al. (2008); Vasquez et al. (2010), and also clearly shown as red contours in the upper-panel of Fig.10 in this paper. The $8.3 \mu\text{m}$ emission is dominated by PAH emission and indicates the presence of PDRs (Vasquez et al. 2010). IRAC $8 \mu\text{m}$ emission shown in color scale in the lower panel of Fig.10 also reveals a shell-like structure of PAH emission.

In Fig.11, we analyze the distribution of the normalized intensities of ^{12}CO (1-0) emission,

HI emission, 1.4 GHz radio emission observed by CGPS and PAH emission revealed by MSX A band along four orientations centered on the Wolf-Rayet star HD 211853. At first glance, one can see that ^{12}CO (1-0) emission and PAH emission encircle an hollow with a angular radius of $\sim 5'$ in each panel, where their emissions are suppressed but 1.4 GHz radio emission enhanced, indicating the central region is filled with UV radiation, which has photodissociated and ionized the molecular and atomic gas. The central Wolf-Rayet star is surrounded by the ionized gas and shows strong continuum emission at $8.3 \mu\text{m}$. The HI emission always shows opposite distribution to the 1.4 GHz radio emission. In other words, the peaks and troughs of HI emission always correspond to the troughs and peaks of the 1.4 GHz radio emission, respectively. This anti-correlation is more significant in the $\text{PA}=0^\circ$ plot. However, we also noticed the HI emission is also high in some regions filled with ionized gas, such as in NVSS 1 and 3. This may be caused by the non-uniform distribution of HI gas, or the projection of the atomic gas located at the outer layer of the expanding bubble. The peaks of ^{12}CO (1-0) emission generally locate outside of PAH emission. The fact that PAH emission locates at the interface between the ionized and molecular material suggests that molecular gas is being photodissociated by the UV photons, i.e., the presence of PDRs (Vasquez et al. 2010). At the radius of $\sim 5'$ in the $\text{PA}=135^\circ$ panel, ^{12}CO (1-0), HI, 1.4 GHz radio and PAH emissions nearly all reach their maximum emissions. This position corresponds to molecular core "A", which is a bright Rimmed cloud and is forming the youngest star cluster in this region (Saurin et al. 2010).

3.3. SEDs of YSOs

Qiu et al. (2008) identified tens of Young Stellar Objects (YSOs) in the south-east of this region. We selected 64 of these sources for analysis. The others are beyond $5'$ from the Wolf-Rayet star HD 211853 and mostly classified as class II objects. The SEDs of these YSOs are then modeled using an online 2D-radiative transfer tool developed by Robitaille et al. (2006,

2007). As input parameters, the distances of these YSOs and the visual extinction A_v were explored in a parameter space of [2.75,3.25] kpc and [2,2.5] mag, respectively. The adopted input A_v is similar to that of HD 211853 (2.28 mag) and BD+55°2722 (2.26 mag) (Vasquez et al. 2010). The SED models, which satisfy the criterion of $\chi^2 - \chi_{best}^2 < 3 \times n_{data}$, where n_{data} is the number of the data points, are accepted and analyzed. Figure 12 shows the SEDs of ten stars.

Following Grave & Kumar (2009), a weighted mean and standard deviation are derived for all the physical parameters of each source from the selected models, with the weights being the inverse of the χ^2 of each model. The fitting results are listed in Table 4. The various columns in Table 4. are as follows: [col. 1] name of the star; [col. 2] and [col. 3] coordinate of the star; [col. 4] number of models averaged; [col. 5] weighted χ^2 ; [col. 6] distance of the star; [col. 7] interstellar extinction; [col. 8] age of the star; [col. 9] mass of the star; [col. 10] total luminosity of the star; [col. 11] envelope mass; [col. 12] envelope accretion rate; [col. 13] disk mass ; [col. 14] disk accretion rate. The evolutionary stages of these YSOs are defined as following (Robitaille et al. 2006): Stage 0/I objects are those with $\dot{M}_{env}/M_* > 10^{-6}yr^{-1}$, Stage II objects are those with $\dot{M}_{env}/M_* < 10^{-6}yr^{-1}$ and $M_{disk}/M_* > 10^{-6}$, and Stage III objects are those with $\dot{M}_{env}/M_* < 10^{-6}yr^{-1}$ and $M_{disk}/M_* < 10^{-6}$. The identifications of the evolutionary stages are listed in the last column of Table 4. "Y14" and "Y20" are badly fitted with χ^2 much larger than 1000, indicating they may not connect to this region. We exclude them in following analysis. The SED of "Y27", which was once classified as class II YSO by Qiu et al. (2008), is more likely from the atmosphere of an evolved star rather than from YSOs. It can be well modeled by a stellar atmosphere with temperature of 7500 K and $\log(g)$ of 0.5. The last panel of Figure 12 presents it's SED. Among the other YSOs, 40% of them are younger than 10^6 yr and 44 have mass smaller than $2 M_\odot$. The youngest and most massive YSOs are found associated with molecular core "A".

One should be careful with these results for individual young stars due to the limit of bands used in fitting. More data especially at long wavelengths are required to better constraint the

properties of these young stars. However, the present results can provide us clues on the age and mass distribution of these young stars spreading in this region. To investigate the reliability of the age and mass distribution of these YSOs in the SED fitting, we fit the SEDs again by loosening the parameter space of A_v , which is explored in [0,2.5] mag. Figure 16 compares the ages and masses of the YSOs in the two runnings. One can find that they coincide with each other very well. So we believe even if the parameters of individual star need to be further constrained, the trend of the age and mass spatial distribution of these YSOs is reliable in statistics.

3.4. The properties of core A / IRAS 22172+5549

Molecular core "A" is associated with IRAS 22172+5549, which is an externally heated rimmed cloud (Qiu et al. 2008). The lower panel of Fig.10 displays the 850 μm emission in red solid contours from SCUBA, which shows a compact dust core. We collected data from IRAS, AKARI and SCUBA, and modeled the SED with wavelength longer than 60 μm , whose emission is mainly from a cool dust envelope, with a simple isothermal gray-body dust model. In the optically thin case, the grey-body dust model can be written as (Zhu et al. 2010; and the references therein):

$$S_\nu \approx \frac{M_{tot}\kappa_\nu B_\nu(T_d)}{gD^2} \quad (1)$$

where S_ν is the continuum emission flux at the frequency ν , M_{tot} is the total mass of gas and dust, κ_ν is the dust opacity per unit dust mass, $g=100$ is the density ratio of gas to dust, D is the distance, and $B_\nu(T_d)$ is the Planck function with a dust temperature of T_d .

For a typical dust coagulation time scale $\tau_{coag} = 10^5$ yr, in the molecular core "A" $n_H \times \tau_{coag} \sim 10^8 \text{ cm}^{-3}\text{yr} < 10^9 \text{ cm}^{-3}\text{yr}$, indicating coagulation does not take considerable effect on the dust opacity in core "A" (Ossenkopf & Henning 1994). Thus the dust opacity of the initial dust distribution (without dust coagulation) with thin ice mantles can be used in the SED fitting (Ossenkopf & Henning 1994). The dust opacity at wavelength λ can be derived as

$\kappa_{\nu} = 0.797 \times \left(\frac{\lambda}{1000\mu\text{m}}\right)^{-1.86}$, which is from fitting the data in Table 1 of Ossenkopf & Henning (1994). Figure 13 shows the SED of IRAS 22172+5549 overlaid by the best fit curve. The dust temperature from the best fit is 26.0 ± 0.6 K, which is larger than the kinematic temperature derived from CO emission, suggesting the dust emission traces a more innermost part than CO gas. The total mass of gas and dust traced by dust emission is $102 \pm 13 M_{\odot}$, which is much smaller than that traced by CO gas. The bolometric luminosity integrated from 20 to $3000 \mu\text{m}$ is $2200 L_{\odot}$. The dust temperature and the bolometric luminosity obtained here are consistent with the dust temperature (28 ± 5 K) and IR luminosity ($2700 L_{\odot}$) calculated only using the measured flux densities at 60 and $100 \mu\text{m}$ (Vasquez et al. 2010).

An embedded infrared cluster "SBB1" is found in this molecular core (Saurin et al. 2010). From SED modeling, nine YSOs younger than 5×10^5 yr are found to be associated with this molecular core, three of which are even younger than 5×10^4 yr, indicating "SBB1" is a very young star cluster. As shown in Figure 12, all the nine YSOs have large infrared excesses. The most three massive ones are "Y54", "Y55" and "Y56", which have a stellar mass $\geq 6 M_{\odot}$. The other six sources have a stellar mass $\leq 3 M_{\odot}$. The infall rate of these nine YSOs is found larger than $\sim 1 \times 10^{-5} M_{\odot} \cdot \text{yr}^{-1}$. "Y57" has the largest infall rate of $\sim 1 \times 10^{-3} M_{\odot} \cdot \text{yr}^{-1}$. All indicate young stars are forming in core "A".

4. Discussion

4.1. The geometry of the ring nebular

The geometry of the ring nebular is important for understanding the interacting between the central Wolf-Rayet star and its environment. In this part, we argue the molecular ring surrounding HD 211853 is more likely flattened rather than spherical. Firstly, there is less molecular emission within the interior of the molecular ring, which excludes the spherical shell hypothesis. Secondly,

from the first moment map of ^{12}CO (1-0) in the left panel of Figure 14, one can find the velocity distribution of the molecular gas is not spherical. The gas is redshifted and blueshifted in the north-east and south-west, respectively. But the gas along NW-SE direction is much less shifted, indicating the molecular gas distributes in a ring with a thickness much smaller than the size of the bubble. The plane in which the molecular ring lies has an inclination angle with respect to the sky plane, leading to the velocity gradient of the molecular gas along NE-SW direction. Finally, as shown in Figure 2, the spectrum of ^{12}CO (1-0) at the position of the WR star only has one velocity component, which excludes two expanding layer hypothesis. The geometry and formation of molecular rings surrounding expanding bubbles have been discussed in detail by Beaumont & Williams (2010). In their interpretation, the morphology of molecular rings naturally arises if the host molecular clouds are oblate, even sheetlike, with thicknesses of a few parsecs. The central massive stars can clear out a cavity in the flattened molecular cloud and create the molecular ring surrounding them. This is just the case of the molecular ring surrounding HD 211853.

A simple geometric model is sketched in the right panel of Figure 14. The axis x and y lie on the plane of the sky. The WR star HD 211853 is located at the origin. The ring nebular is shown as red circle. The projection of the ring nebular in the sky plane is shown as blue ellipse. The lengths of the semimajor and semiminor axis of the ellipse are denoted as "a" and "b". The angle θ is the inclination angle between the plane of the ring nebular and the sky plane. The angle ϕ is the position angle measured from the major axis. From this simple geometric model, the inclination angle θ can be inferred from:

$$\cos \theta = \frac{b}{a} \quad (2)$$

The observed velocity, V_{obs} of a point on the ellipse is given by:

$$V_{obs} = V_{exp} \cdot \delta \cdot \sin \theta \sqrt{\frac{1}{1 + \cos^2 \theta \cdot \cot^2 \phi}} + V_{sys} \quad (3)$$

where V_{sys} is the systemic velocity, V_{exp} is the expanding velocity, $\delta=1$ when $0 \leq \phi \leq 180^\circ$ and

$\delta=-1$ when $180 \leq \phi \leq 360^\circ$. The two dashed ellipse in the left panel of Figure 14 approximately mark the boundary of the interior and exterior of the molecular ring. The inner and outer ellipses are of $4'.5 \times 3'$ and $7' \times 5'$ in diameter. Thus the inclination angle between the plane of the ring nebular and the sky plane turns out to be $\sim 44^\circ - 48^\circ$. From the left panel of Figure 14, the maximum value of $|V_{obs} - V_{sys}|$ is found to be 3.5 km s^{-1} along the direction of the minor axis, indicating an expanding velocity of $\sim 5 \text{ km s}^{-1}$.

As shown in Figure 1, the ring nebular surrounding HD 211853 is part (shell B) of the large HII region Sh2-132. Although shell B is mainly ionized and created by HD 211853, its interacting with the other part (shell A) can not be ignored. The formation of shell B should be affected by the expanding of shell A, especially in the west, where the molecular ring is not closed. In the above toy model, we didn't take into account the interacting with shell A, which needs more detailed modeling. However, the simple model can roughly depict the ring structure surrounding HD 211853 and explain the spatial and velocity distribution of the molecular gas in the ring nebular.

4.2. Gravitational stability of the molecular cores

The gravitational stability of the molecular cores can be investigated by comparing their core masses with virial masses and Jeans masses. Assuming the cloud core is a gravitationally bound isothermal sphere with uniform density and is supported solely by random motions, the virial mass M_{vir} can be calculated following Ungerechts et al. (2000):

$$\frac{M_{vir}}{M_\odot} = 2.10 \times 10^2 \left(\frac{R}{pc}\right) \left(\frac{\Delta V}{km \text{ s}^{-1}}\right) \quad (4)$$

where R is the radius of the core and ΔV is the line width of ^{13}CO (1-0). The virial masses are listed in the 15th column of Table 2.

Many factors including thermal pressure, turbulence, and magnetic field support the gas against gravity collapse in molecular cores. Taking into account of thermal and turbulent support,

the Jeans mass can be expressed as (Hennebelle & Chabrier 2008):

$$M_J = a_J \frac{C_{s,eff}^3}{\sqrt{G^3 \rho}} \quad (5)$$

where a_J is a dimensionless parameter of order unity which takes into account the geometrical factor, ρ is the mass density and $C_{s,eff}$ is an effective sound speed including turbulent support,

$$C_{s,eff} = [(C_s)^2 + (\sigma_{NT})^2]^{1/2} \quad (6)$$

where C_s is the thermal sound speed and σ_{NT} is the non-thermal one dimensional velocity dispersion. The thermal sound speed is related with the kinematic temperature: $C_s = (kT_k/\mu_g m_{H_2})^{1/2}$, where $\mu_g=1.36$ is the mean atomic weight of the gas. The non-thermal one dimensional velocity dispersion σ_{NT} can be calculated as following:

$$\sigma_{NT} = \sqrt{\sigma_{^{13}CO}^2 - \frac{kT_k}{m_{^{13}CO}}} \quad (7)$$

and

$$\sigma_{^{13}CO} = \frac{\Delta V}{\sqrt{8 \ln(2)}} \quad (8)$$

with $m_{^{13}CO}$ is the mass of ^{13}CO . By introducing an effective kinematic temperature $T_{eff} = \frac{C_{s,eff}^2 \mu_g m_{H_2}}{k}$, equation (5) can be rewritten in a similar form as equation (18) in Hennebelle & Chabrier (2008),

$$M_J \approx 1.0 a_J \left(\frac{T_{eff}}{10 \text{ K}}\right)^{3/2} \left(\frac{\mu}{2.33}\right)^{-1/2} \left(\frac{n}{10^4 \text{ cm}^{-3}}\right)^{-1/2} M_\odot \quad (9)$$

where n is the volume density of H_2 calculated with Radex, μ is the mean molecular weight of the gas. The Jeans masses calculated are listed in the 16th column of Table 2.

The core masses of core "C", "E", and "H" are found much smaller than their virial masses and Jeans masses. While the core masses of the other cores are comparable with their virial masses and Jeans masses. To keep in mind, we didn't consider the external pressure from their ionized boundary layers in calculating the virial masses and Jeans masses above. It seems these cores are gravitationally stable against collapse without external pressure. However, the rising

external pressure surrounding them can significantly change their stabilities and induce collapse in them (Thompson et al. 2004). The external pressure from the ionized layer is (Morgan et al. 2004):

$$\frac{P_{ext}}{k} = 2\rho_i C_i^2 = 4n_e T_e \quad (10)$$

The effective electron temperature T_e is assumed to be 8000 K. The electron densities n_e in the ionized boundary layers surrounding core "A", "B", and "G" are taken as the values of NVSS sources 5, 4, and 1, respectively. For the other cores, we assume n_e to be 20 cm^{-3} (Vasquez et al. 2010). The calculated external pressure from the ionized layers can be found in the 18th column in Table 2. Molecular pressure inside the clouds can be expressed as:

$$\frac{P_{mol}}{k} = n T_{eff} \quad (11)$$

The inferred P_{mol} can be found in the last column of Table 2. We can see for all the cores, the external pressure from the surrounding ionized gas is much larger than the molecular pressure, indicating the photoionisation induced shocks can penetrate into the interiors of the molecular cores and compress materials inside (Morgan et al. 2004). To explore the stabilities of these cores subject to non-negligible external pressure, we calculated the "pressurised virial mass" as (Thompson et al. 2004):

$$M_{pv} \simeq 5.8^{-2} \frac{(\Delta V)^4}{G^{3/2} P_{ext}^{1/2}} \quad (12)$$

where G is the gravitational constant and ΔV is the line width of ^{13}CO (1-0) lines. The calculated "pressurised virial masses" are listed in the 17th column of Table 2. The molecular cores with core masses exceeding their "pressurised virial mass" are unstable against gravitational collapse (Thompson et al. 2004). Core "C", "E" and "H" have core masses smaller than their "pressurised virial mass", indicating they are stable even under external pressure. For the other cores, their core masses are much larger than their "pressurised virial mass", suggesting they are likely to be unstable against collapse. It can be seen the high external pressure has a great destabilizing effect upon the gravitational stabilities of the cores.

4.3. The effect of the Wolf-Rayet star on the molecular distribution

It is expected the current WR stars and their previous main sequence phase should greatly influence on their associated cloud. Vasquez et al. (2010) has demonstrated that the mechanical energy released by the Wolf-Rayet star HD 211853 can shape the ring-like structure of the molecular and PAH distributions.

From equation (3), one can see the gases distributed along a direction of a given position angle should have the same observed velocity. However this is not true in the first moment map in the left panel of Figure 14. Instead, one can notice the expanding velocity increases with the distance from the origin, especially for the gases along NE-SW direction. This situation can be also found in the PV diagrams in Figure 6, where the velocity distribution shows a "Hubble law". Such velocity gradient was also noticed in the molecular clouds surrounding O stars (Dent et al. 2009). It seems the expansion of the ionized gas can constantly accelerate the molecular gas. However, the acceleration is not significant towards the dense cores as shown in Fig.8. The dense molecular cores seem to have slightly velocity deviation from the systemic velocity, which can be explained that the expansion of the ionized gas decelerated by the resistance of the dense cores due to their large column densities. Anyway, HD 211853 has significant effect on its surrounding molecular gas by sweeping, photodissociating, reshaping and possibly collecting.

We also noticed that infrared point sources in the molecular ring always separated from the molecular cores. This effect is more significant towards core "C" and "F", where the infrared sources locate in front of the molecular core and face the central Wolf-Rayet system, indicating the molecular cores have different expanding velocities with the infrared point sources. This separation indicates that stellar wind has different effect on dust and gas. However, such separation maybe caused by the moving out of the formed stars from their parent clouds during evolution or by inducing new cores by those formed stars. Detailed analysis and observations are needed to settle this problem.

4.4. Sequential star formation in the vicinity of core "A"

4.4.1. Large-scale sequential star formation

YSOs with various ages are drawn with different markers in Fig.15 overlaid on the column density of H_2 in grey and excitation temperature of ^{12}CO (1-0) in contours. The interesting thing is that the age gradient of the YSOs appears in a large-scale. The oldest YSOs with ages larger than 2×10^6 yr are scattered in a large area from the Wolf-Rayet system to the molecular ring. The younger ones with ages larger than 5×10^5 yr but smaller than 10^6 yr locate in the midway, while the youngest ones are found associated with molecular core "A". Such age gradient can also be identified in panel (i) of Figure 2 in Qiu et al. (2008). In their paper, the evolutionary stages of the YSOs in this region are identified in color-color diagrams.

We averaged the ages of the YSOs in each $0.5'$ radius bin and presented the radial age distribution in Fig.17. The projection effect was not taken account. Since the YSOs mainly distribute in the vicinity of core "A", the projection effect should not greatly affect the trend of the age distribution. We find the YSOs within $2'$ from the Wolf-Rayet system are as old as 2×10^6 yr. Those between $2'$ and $4'$ are with ages $\sim 1.2 \times 10^6$ yr. The youngest stars are beyond $4'$ and with an average age of $\sim 2 \times 10^5$ yr. It is clearly to see the nearer YSOs are older than the further ones, indicating a stellar age gradient. The stellar age distribution suggests at least three generations of stars have been forming in this region. The oldest generation is closer to the Wolf-Rayet system, while the youngest one locates in the molecular ring. In addition, the three star clusters in this region have different ages (Saurin et al. 2010). The "Teutsch 127", which includes the O-type star BD+55°2722 and near the Wolf-Rayet star HD 211853, is the oldest one (~ 5 Myr). The "SBB 2" is as old as ~ 2 Myr. The age of the youngest cluster "SBB 1" is about 1 Myr. The age gradient of these three star cluster also indicates sequential star formation in a large scale. Such "relay star formation" is a hint of triggered star formation due to expansion of bubbles created by stellar wind of massive stars (Chen et al. 2007).

4.4.2. *Small-scale sequential star formation*

As shown in Fig.15, a small-scale age gradient is found associated with molecular core A, a bright rimmed cloud. The older and less massive YSOs embrace the molecular core, while the youngest and more massive stars reside deeper into the core. This picture is in accordance with the so-called "radiation-driven implosion" (RDI) process as depicted in Figure 1 of Ogura (2006), which is proposed for triggered star formation in bright rimmed cloud (Bertoldi 1989; Bertoldi & McKee 1990). In the model, the surface layer of the cloud is ionized by the UV photons from massive stars and then the cloud is compressed and collapses due to the shock generated from the ionization front. As discussed in section 4.2, core A is likely to collapse due to the external pressure from the ionized boundary layer. Recent simulation suggests there is a range of ionising fluxes in the RDI model, that trigger star formation in the bright rimmed cloud (Bisbas et al. 2011). This range is about $10^9 \text{cm}^{-2} \text{s}^{-1} \lesssim \Phi_{\text{LyC}} \lesssim 3 \times 10^{11} \text{cm}^{-2} \text{s}^{-1}$. If the ionising flux is larger than $10^9 \text{cm}^{-2} \text{s}^{-1}$, the shock front preceding the D-type ionization front can propagate into the cloud, compress it, and trigger star formation therein (Bisbas et al. 2011). However large ionising flux can rapidly disperse the cloud without triggering star formation (Bisbas et al. 2011). The ionising fluxes surrounding core "A" can be estimated as (Morgan et al. 2004):

$$\Phi_{\text{LyC}} = 1.24 \times 10^{10} S_{\nu} T_e^{0.35} \nu^{0.1} \theta^{-2} \quad (13)$$

where S_{ν} is the integrated radio flux in mJy, T_e is the effective electron temperature of the ionised gas in K, ν is the frequency in GHz and θ is the angular diameter over which the emission is integrated in arcseconds. Assuming $T_e = 8000$ K, the ionising flux in NVSS 5 is inferred as $1.1 \times 10^{10} \text{cm}^{-2} \text{s}^{-1}$, which is taken as the value in the ionizing boundary layer surrounding core "A". This value is moderate, indicating triggered star formation can take place in core "A". But in the simulation of Bisbas et al. (2011), the RDI model favors formation of low mass stars in the clouds, which contradicts the situation in core "A", where YSOs with masses larger than $6 M_{\odot}$ are found. We noticed the initial cloud mass in their simulation is much smaller than the mass of

core "A", which may be responsible for the contradiction. Additionally, other processes such as "collect and collapse" may also play an important role in the star formation in core "A", which will be discussed in the next section.

4.5. Collect and Collapse scenario

The ring-like structure of dust and gas distribution and the existence of PDR indicate the star formation in this region favor the "Collect and Collapse" scenario (Deharveng, Zavagno, & Caplan 2005; Vasquez et al. 2010). The molecular ring is composed of well separated, dense and massive cores, most of which are under collapsing. Such regular spacing rule of the cores could not be pre-existing clumps but be formed by external triggering, which is a strong evidence for the "collect and collapse process" (Deharveng, Zavagno, & Caplan 2005; Ogura 2010). This situation contradict the RDI model, in which the dense clumps the radiatively induced shocks drive into are pre-existing. Additionally, the large scale sequential star formation discussed in section 4.4.1 also favors the "Collect and Collapse" process rather than "RDI" model (Elmegreen & Lada 1977; Ogura 2010).

However, as discussed in section 4.4.2, the bright rimmed nebular core "A" also seems to favor the "RDI" model. But the "Collect and Collapse" process and the "Radiation Driven Implosion" process can not take place at the same time and place. To resolve this contradiction, we propose that these two processes may function at different time in this region. Firstly, neutral materials are collected and accumulated into a dense shell between the ionization front (IF) and shock front (SF) generated by the expanding HII region. Secondly, the compressed shocked layer becomes gravitationally unstable and fragments into regularly spaced massive clumps on a long time scale. These two steps are just like the "Collect and Collapse" process. Thirdly, the clumps are illuminated and eroded by the ionization front, leading to the formation of bright rims and/or cometary globules, which collapse to form stars due to external pressure as discussed in

section 4.2. The third step is like the "RDI" process. Besides, the ionization front illuminating the bright rimmed nebular core "A" is more likely generated from young cluster "SBB 2" rather than from the central Wolf-Rayet star (Saurin et al. 2010). Relatively speaking, core "A" is pre-existing comparing with the ionization front generated from the older cluster. In addition, a possible bow-shock seems to have been generated in the cluster "SBB 2" and impact on "SBB 1" (Saurin et al. 2010). So we suggest the star formation in core "A" may be also affected by the older cluster "SBB 2" through a process like "RDI", leading to form the youngest embedded star cluster "SBB 1".

4.6. Comparing with the other star forming regions

It is necessary to compare the characters of the molecular cores in this region with the other star forming regions. The line width of ^{13}CO (1-0) ranges from 1.3 to 2.6 km s^{-1} with a mean value of 2.1 km s^{-1} , which is very similar to that of intermediate-mass star forming regions (~ 2 km s^{-1}) (Liu et al. 2011; Sun et al. 2006), larger than that of low-mass star forming regions (~ 1.3 km s^{-1}) (Myers, Linke & Benson 1983), but much smaller than that of high-mass star forming regions associated with IRAS sources (> 3 km s^{-1}) (Wang et al. 2009; Wu et al. 2003, 2001) or methanal masers (~ 4.5 km s^{-1}) (Liu et al. 2010). Judging from the line width of ^{13}CO (1-0) in this region, the molecular cores where triggered star formations possibly take place favor to form intermediate-mass YSOs, which is confirmed by SED modeling to the YSOs in molecular core A. As discussed in section 4.4.2, core A is suggested to suffer a "radiation-driven implosion" (RDI) process. A tendency for HAeBe stars forming deeper into the cloud is expected in RDI model (Ogura 2006; Chen et al. 2007). Liu et al. (2011) have found that the regions harboring HAeBe stars younger than 10^6 yr are with an average column density of $\sim 5 \times 10^{21}$ cm^{-2} , which are slightly smaller than that in most cores of this region. They also got an average excitation temperature ~ 16 K in those HAeBe regions younger than 10^6 yr, which are slightly smaller than

that in the molecular cores of this region (~ 20 K), indicating the influence of external heating.

5. Summary

We studied the environment surrounding Wolf-Rayet star HD 211853 in molecular emission, infrared emission, as well as radio and HI emission. The SEDs of the YSOs which are located in the south-east part of this region are modeled with an on line YSO SED fitting tool. Triggered star formation are discussed. The main findings of this paper are as following:

(1). The molecular emission has two components. One peaks at -50 km s $^{-1}$, which is likely from a foreground cold cloud. The other one has a systemic velocity of -43.5 km s $^{-1}$, whose ^{13}CO (1-0) emission forms a ring-like structure with several well separated molecular cores. The line width of ^{13}CO (1-0) ranges from 1.3 to 2.6 km s $^{-1}$ with a mean value of 2.1 km s $^{-1}$, which is very similar to that of intermediate-mass star forming regions.

(2). The properties of the molecular cores are analyzed under LTE assumption as well as with non-LTE models in RADEX. Both LTE and non-LTE analysis give the same excitation temperatures of ^{12}CO (1-0) (~ 20 K). The excitation temperatures of ^{13}CO (1-0) calculated with RADEX are much smaller than that of ^{12}CO (1-0). The core masses calculated under LTE and non-LTE are similar, ranging from $\sim 10^2$ to $\sim 10^3$ M_{\odot} . The volume densities of H_2 in this cores are of $\sim 10^3$ cm $^{-3}$.

(3). The molecular emission is associated with $8.3\mu\text{m}$ emission in MSX A band. We also witnessed structures like cavities and shells in HI emission. Radio emission at 1.4 GHz is embraced by the molecular and dust ring. Ionization fronts can be easily identified between the radio and molecular emission especially in the south-east part.

(4). We find that the molecular gas surrounding HD 211853 is not spherically expanding. The molecular gas distributes in a ring-like structure with a thickness much smaller than the size

of the bubble. The inclination angle between the plane of the ring nebular and the sky plane turns out to be $\sim 44^\circ - 48^\circ$. The expanding velocity of the ring nebular is about $\sim 5 \text{ km s}^{-1}$. The expanding velocity seems to increase with the distance from the WR star.

(5). The molecular cores are well separated along the ring. It seems these cores are gravitationally stable against collapse without external pressure. But the high external pressure from the ionized gas has a great destabilizing effect upon the gravitational stabilities of the cores. Core "C", "E" and "H" have core masses smaller than their "pressurised virial mass", indicating they are stable even under external pressure. For the other cores, their core masses are much larger than their "pressurised virial mass", suggesting they are likely to be unstable against collapse.

(5). From the SED modeling of the YSOs located in the south-east of HD 211853, a stellar age gradient is found across a large scale in space from the Wolf-Rayet star to the molecular ring. The presence of PDR, the fragmentation of the molecular ring, the collapse of the cores, the large scale sequential star formation indicate the "Collect and Collapse" process can work in this region.

(6). Molecular core A is forming a star cluster as young as $\sim 10^5$ yr. Core A is embraced by the ionization front and older less massive YSOs. More massive YSOs are forming deeper into core A. The ionizing flux from the ionized boundary layer surrounding core "A" is moderate enough to generate a leading shock, which propagates into the cloud, compresses it, and triggers star formation therein. This is very similar to the picture depicted by the "Radiation-Driven Implosion" models.

In conclusion, the star formation in the molecular ring is induced by the Wolf-Rayet star HD 211853 through the interacting between the expanding ionizing gas and the ISM. The evolution of the molecular ring and the triggered star formation may be affected by both "Collect and Collapse" and "Radiation-Driven Implosion" processes. Generally speaking, the materials in the host molecular cloud surrounding the WR star are collected into a molecular ring. Then the ring fragments into well separated cores, which favor the "Collect and Collapse" process.

The cores are unstable due to external pressure and collapse inside to form stars. The ionization front proceeded by a shock front generated from older star cluster (like "SBB 2") can propagate into the cloud (core "A") and compress it and trigger star formations therein as depicted by the "radiation-driven implosion" process.

Acknowledgment

We are grateful to the staff at the Qinghai Station and Key Laboratory for Radio Astronomy of PMO, CAS, for their assistance during the observations. This work was partly supported by the NSFC under grants No. 11073003, 10733030, and 10873019, and by the National key Basic Research Program (NKBRP) No. 2007CB815403 and No. 2012CB821800.

REFERENCES

- Beaumont, C. N., & Williams, J. P., 2010, 709, 791
- Bertoldi, F. 1989, ApJ, 346, 735
- Bertoldi, F. & McKee, C. F. 1990, ApJ, 354, 529
- Bisbas, T. G., Wunsch, R., Whitworth, A. P., Hubber, D. A., Walch, S., 2011, ApJ, 736, 142
- Brand, J., Massi, F., Zavagno, A., Deharveng, L., Lefloch, B., 2011, A&A, 527, 62
- Cappa, C. E., Vasquez, J., Arnal, E. M., Cichowolski, S., Pineault, S., 2008, RMxAC, 33, 142
- Chen, W. P., Lee, H. T., Sanchawala, K., 2007, IAUS, 237, 278
- Conti P. S., Vacca W. D., 1990, AJ, 100, 431
- Condon, J. J., Cotton, W. D., Greisen, E. W., Yin, Q. F., Perley, R. A., et al., 1998, AJ, 115, 1693
- Dent, W. R. F., Hovey, G. J., Dewdney, P. E., Burgess, T. A., Willis, A. G., et al., 2009, MNRAS, 395, 1805
- Deharveng, L., Lefloch, B., Zavagno, A., Caplan, J., Whitworth, A. P., et al. 2003, A&A, 408, L25
- Deharveng, L., Zavagno, A., & Caplan, J., 2005, A&A, 433,565
- Deharveng, L., Lefloch, B., Kurtz, S., Nadeau, D., Pomarès, M., et al., 2008, A&A, 482, 585
- Di Francesco, J., Johnstone, D., Kirk, H., MacKenzie, T., Ledwosinska, E., 2008, ApJS, 175, 277
- Elmegreen, B. G., & Lada, C. J. 1977, ApJ, 214, 725
- Garden, R. P., Hayashi, M., Hasegawa, T., Gatley, I., Kaifu, N., 1991, ApJ, 374, 540
- Grave J. M. C. & Kumar M. S. N., 2009, A&A, 498, 147
- Gritschneder, M., Naab, T., Burkert, A., Walch, S., Heitsch, F., et al., 2009, MNRAS, 393, 21

- Guilloteau, S. & Lucas, R., 2000, in *Astronomical Society of the Pacific Conference Series*, Vol. 217, *Imaging at Radio through Submillimeter Wavelengths*, ed. J. G. Mangum & S. J. E. Radford, 299
- Harten R. H., Felli M., Tofani G., 1978, *A&A*, 70, 205
- Haworth, T. J. & Harries, T. J., 2012, *MNRAS*, 420, 562
- Hennebelle, P., & Chabrier, G., 2008, *ApJ*, 684, 395
- Hester, J. J., & Desch, S. J. 2005, *ASP Conf. Ser. 341: Chondrites and the Protoplanetary Disk*, 341, 107
- Lefloch B., & Lazareff, B., 1994, *A&A*, 289, 559
- Li, D., & Goldsmith, P. F. 2003, *ApJ*, 585, 823
- Liu, T., Wu, Y.-F., Wang, K., 2010, *RAA*, 10, 67
- Liu, T., Zhang, H. W., Wu, Y. F., Qin, S.-L., Miller, M., 2011, *ApJ*, 734, 22
- Marston, A. P., 1996, *AJ*, 112, 2828
- Martín-Pintado, J., Gaume, R. A., Rodríguez-Fernández, N., de Vicente, P., Wilson, T. L., 1999, *ApJ*, 519, 667
- Meynet G., Maeder A., 2005, *A&A*, 429, 581
- Miao J., White G. J., Thompson M. A., Nelson R. P., 2009, *ApJ*, 692, 382
- Morgan, L. K., Thompson, M. A., Urquhart, J. S., White, G. J., Miao, J., 2004, *A&A*, 426, 535
- Morgan, L. K., Figura, C. C., Urquhart, J. S., Thompson, M. A., 2010, *MNRAS*, 408, 157
- Myers, P. C., Linke, R. A., & Benson, P. J., 1983, *ApJ*, 264, 517
- Nishimaki, Y., Yamamuro, T., Motohara, K., Miyata, T., Tanaka, M., 2008, *PASJ*, 60, 191
- Ogura, Katsuo., 2006, *BASI*, 34, 1110

- Ogura, K., 2010, *ASInC*, 1, 190
- Ossenkopf, V., & Henning, T. 1994, *A&A*, 291, 943
- Panagia, N. & Walmsley, C. M., 1978, *A&A*, 70, 411
- Petriella, A., Paron, S., & Giacani, E. 2010, *A&A*, 513, A44+
- Pomarès, M., Zavagno, A., Deharveng, L., Cunningham, M., Jones, P., et al., 2009, *A&A*, 494, 987
- Price, S. D., Egan, M. P., Carey, S. J., Mizuno, D. R., Kuchar, T. A., 2001, *AJ*, 121, 2819
- Qiu, Keping., Zhang, Qizhou., Megeath, S. Thomas., Gutermuth, Robert A., Beuther, Henrik., et al, 2008, *ApJ*, 685, 1005
- Robitaille T. P., Whitney B. A., Indebetouw R., Wood K., & Denzmore P., 2006, *ApJS*, 167, 256
- Robitaille T. P., Whitney B. A., Indebetouw R., and Wood K., 2007, *ApJS*, 169, 328
- Saurin, T. A., Bica, E., & Bonatto, C., 2010, *MNRAS*, 407, 133
- Shan, W., Li, Z., Zhong, J., Shi, S., 2009, *IEEE Trans. On Appl. Supercond*, 19, 432.
- Sharpless S., 1959, *ApJS*, 4, 257
- Sugitani, K., Fukui, Y., Ogura, K., 1991, *ApJS*, 77, 59
- Sugitani, K., & Ogura, K., 1994, *ApJS*, 92, 163
- Sun, K., Kramer, C., Ossenkopf, V., Bensch, F., Stutzki, J., et al., 2006, *A&A*, 451, 539
- Taylor, A. R., Gibson, S. J., Peracaula, M., Martin, P. G., Landecker, T. L., et al., 2003, *AJ*, 125, 3145
- Thompson, M. A., White, G. J., Morgan, L. K., Miao, J., Fridlund, C. V. M., et al., 2004, *A&A*, 414, 1017
- Ungerechts H., Umbanhowar P., & Thaddeus P., 2000, *ApJ*, 537, 221
- Urquhart J. S., Thompson M. A., Morgan L. K., White G. J., 2004, *A&A*, 428, 723

- Urquhart J. S., Thompson M. A., Morgan L. K., White G. J., 2006, *A&A*, 450, 625
- Urquhart J. S., Thompson M. A., Morgan L. K., Pestalozzi M. R., White G. J., Muna D. N., 2007, *A&A*, 467, 1125
- Van der Tak, F.F.S., Black, J.H., Schöier, F.L., Jansen, D.J., van Dishoeck, E.F. 2007, *A&A*, 468, 627
- Vasquez, J., Cappa, C. E., Pineault, S., Duronea, N. U., 2010, *MNRAS*, 405, 1976
- Wang, K., Wu, Y. F., Ran, L., Yu, W. T., Miller, M., 2009, *A&A*, 507, 369
- Whitworth, A. P., Bhattal, A. S., Chapman, S. J., Disney, M. J., & Turner, J. A. 1994, *MNRAS*, 268, 291
- Wu, Y., Wang, J., & Wu, J., 2003, *Chin. Phys. Letter*, 20, 1409
- Wu, Y., Wu, J., Wang, J., 2001, *A&A*, 380, 665
- Zavagno, A., Deharveng, L., Comerón, F., Brand, J., Massi, F., et al., 2006, *A&A*, 446, 171
- Zavagno, A., Pomarès, M., Deharveng, L., Hosokawa, T., Russeil, D., et al., 2007, *A&A*, 472, 835
- Zhu, L., Wright, M. C. H., Zhao, J-H., Wu, Y. F., 2010, *ApJ*, 712, 674

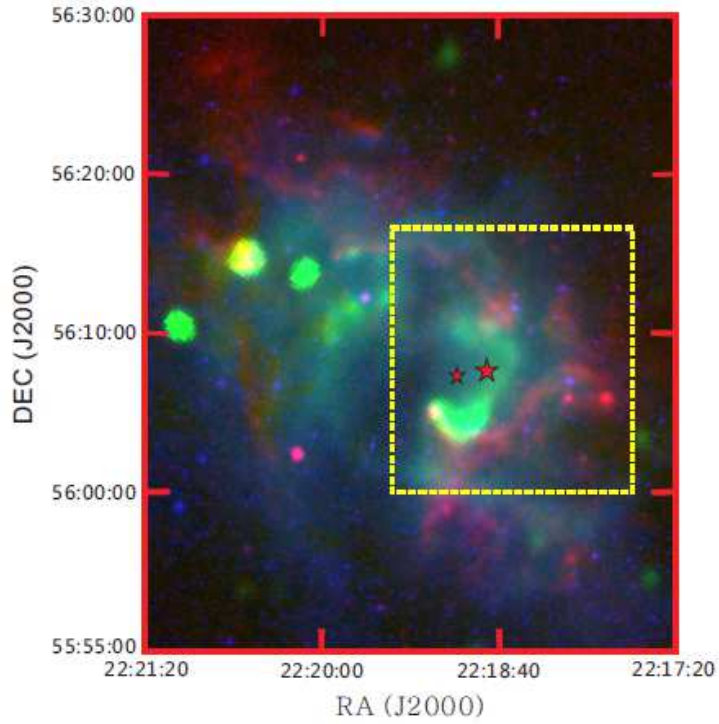


Fig. 1.— A composite color image in this region: DSS2-R optical emission is in blue, 1420 GHz radio emission detected in CGPS in green, and 8.3 μm emission detected at MSX A band in red. The larger "star" shows the location of the WR star HD 211853 and the small "star" represents the position of the massive O-type star BD+55°2722. The yellow dashed "box" shows the region of Shell B, which is focused in this paper.

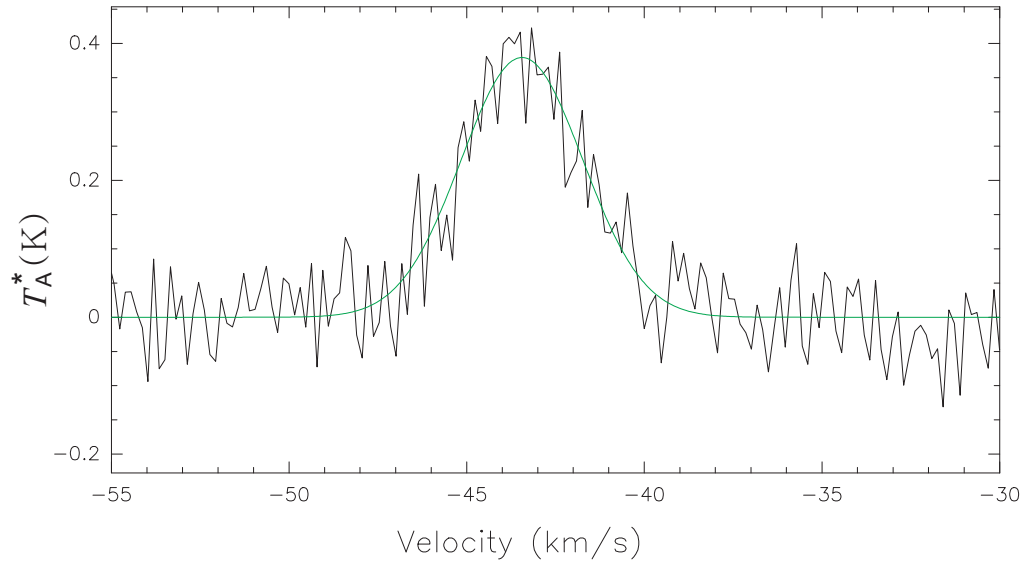


Fig. 2.— Spectrum of ^{12}CO (1-0) at the position of the Wolf-Rayet star HD 211853 averaged over $1'$. The green solid line is the gaussian fit curve.

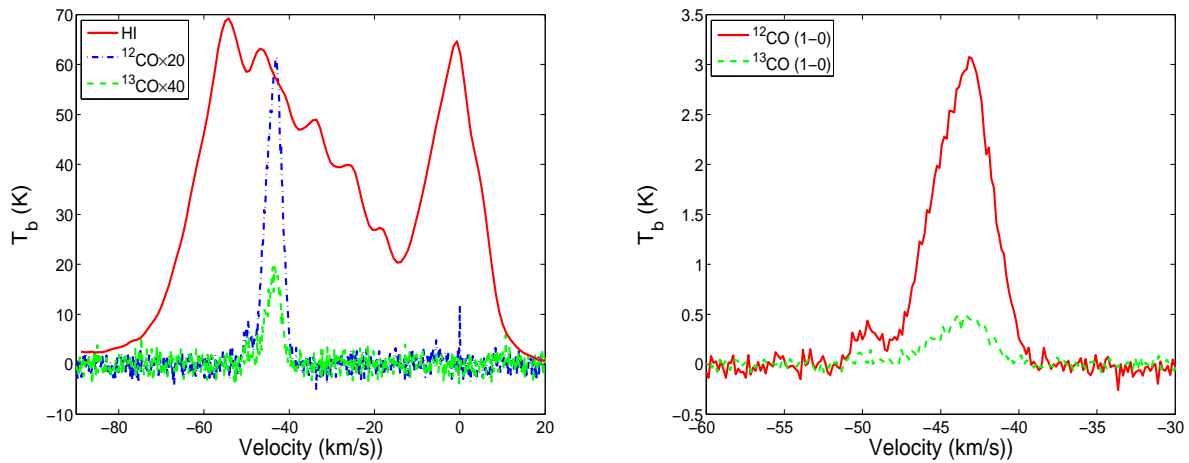


Fig. 3.— Left: Spectra of ^{12}CO (1-0), ^{13}CO (1-0) and HI averaged over an area of $14' \times 14'$ centered at the Wolf-Rayet star HD 211853. Right: Zoomed in averaged spectra of ^{12}CO (1-0), ^{13}CO (1-0).

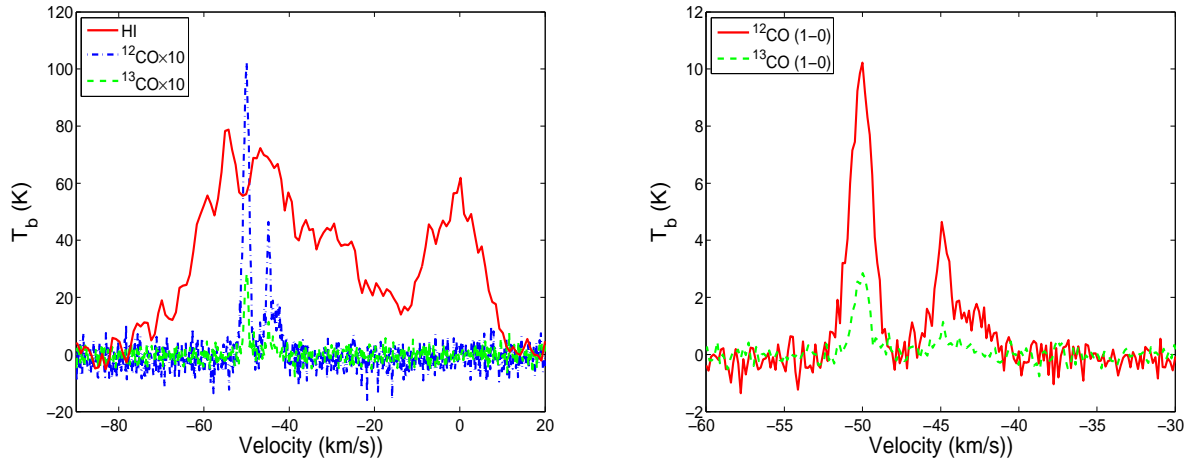


Fig. 4.— Left: Spectra of $^{12}\text{CO} (1-0)$, $^{13}\text{CO} (1-0)$ and HI taken from the emission peak of the component at -50 km/s (core "T"). Right: Zoomed in spectra of $^{12}\text{CO} (1-0)$, $^{13}\text{CO} (1-0)$ at core "T".

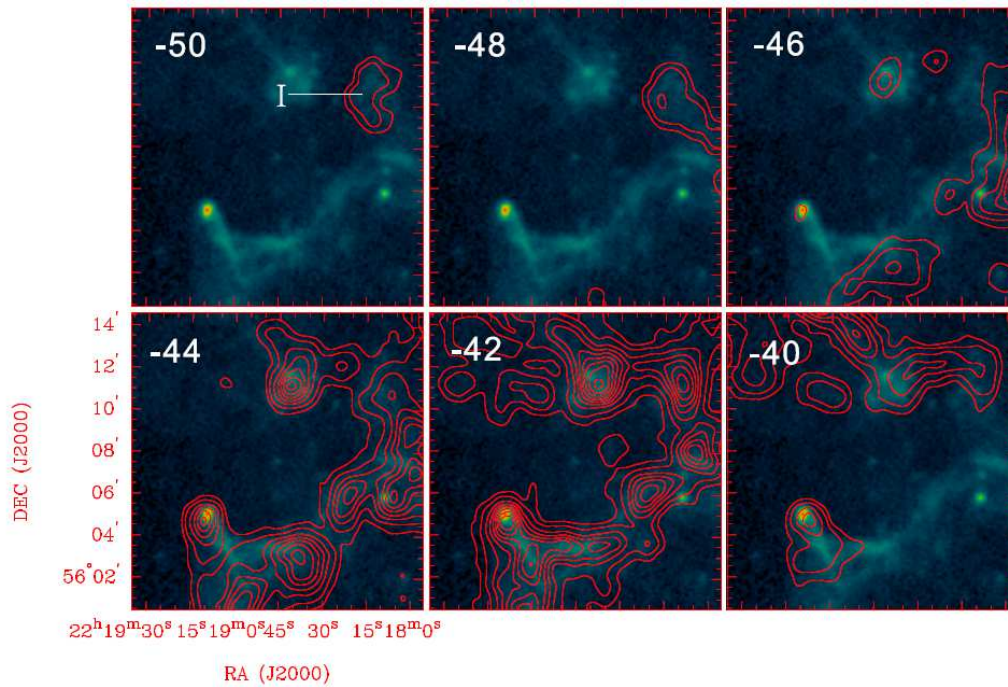


Fig. 5.— Channel maps of ^{12}CO (1-0). The middle velocities are plotted on the upper-right corners of each panel. The integrated velocity interval in each panel is $2\ \text{km s}^{-1}$. The contours are from 20% to 90% of the peak intensity ($4.6\ \text{K}\cdot\text{km s}^{-1}$). The background image shows the $8.3\ \mu\text{m}$ emission detected at MSX A band. The position of core "I" is marked in the $-50\ \text{km s}^{-1}$ panel.

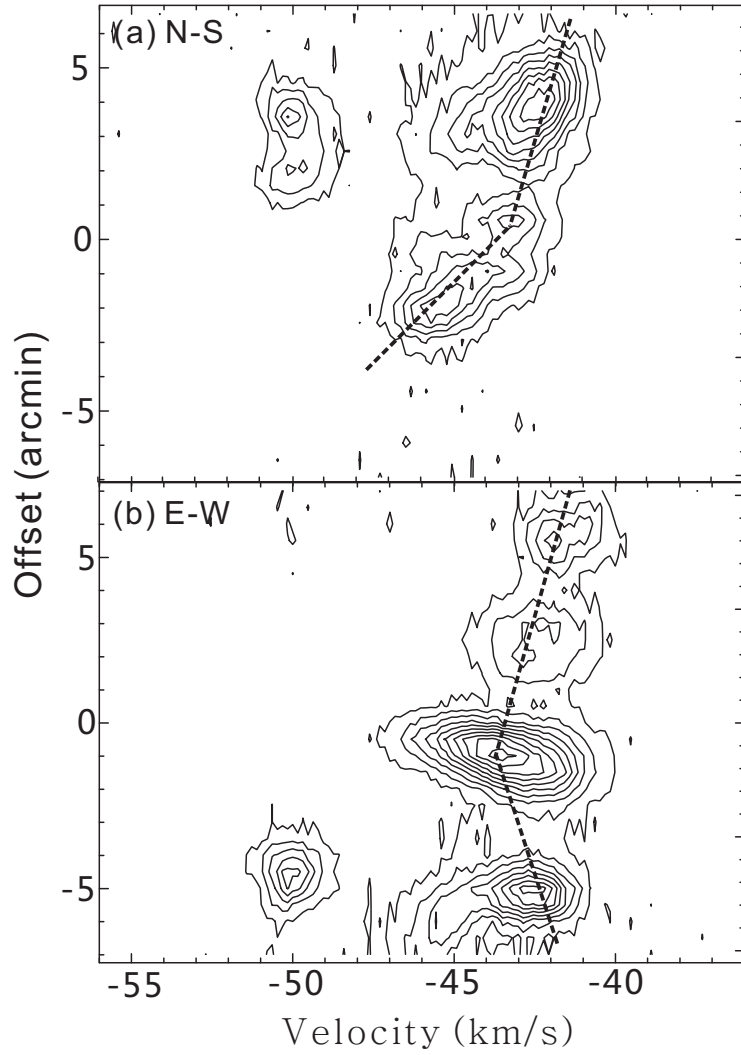


Fig. 6.— PV diagrams of ^{12}CO (1-0) cut along the orientations denoted in Fig.7. The contours are from 0.6 K (3σ) in steps of 1 K.

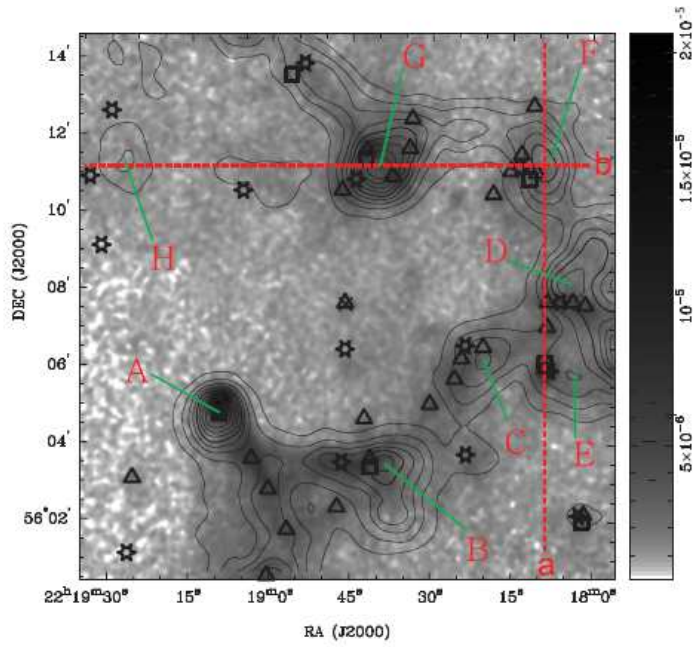


Fig. 7.— ^{13}CO (1-0) integrated intensity map overlaid on MSX A band emission. The contours are from 10% to 90% of the peak ($7.8 \text{ K} \cdot \text{km s}^{-1}$). ”Triangles” represent MSX point sources, ”boxes” IRAS point sources, and ”stars” AKARI point sources. The Wolf-Rayet star is drawn as ”cross”. The molecular cores are denoted from ”A” to ”H”. The horizon and vertical dashed lines represent the directions of the P-V cuts in Fig.6.

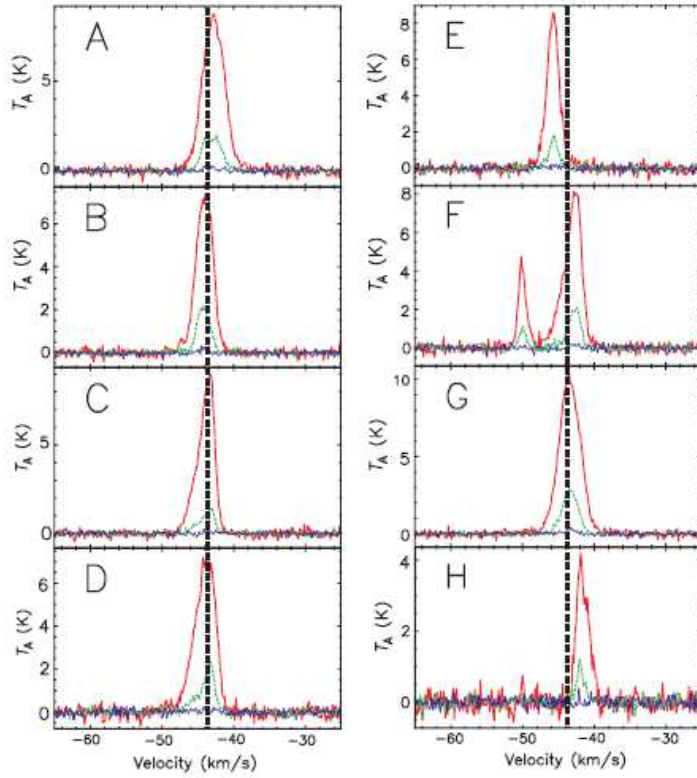


Fig. 8.— Spectra of ^{12}CO (1-0) are in red, those of ^{13}CO (1-0) in green and C^{18}O (1-0) in blue. The core names are labeled on the upper-left corners of each panel. The dashed black lines indicate the systemic velocity of -43.5 km s^{-1} .

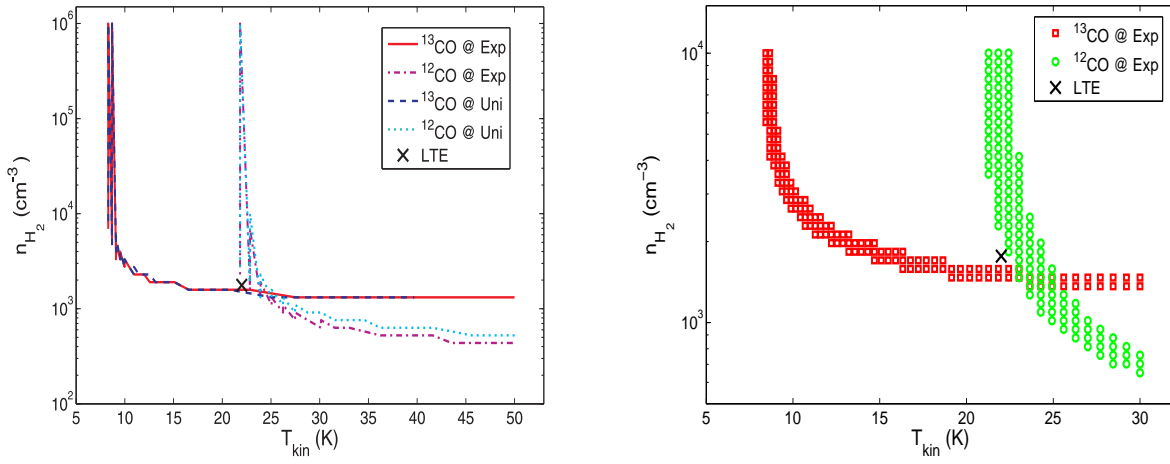


Fig. 9.— Non-LTE model fitting of the ^{12}CO (1-0) and ^{13}CO (1-0) at the emission peak of core A. Left: parameters run through T_{kin} of [5,50] K and n_{H_2} of [$10^2, 10^6$] cm⁻³ in log space. Right: parameters run through T_{kin} of [8,30] K and n_{H_2} of [$2.5 \times 10^2, 10^4$] cm⁻³ in log space.

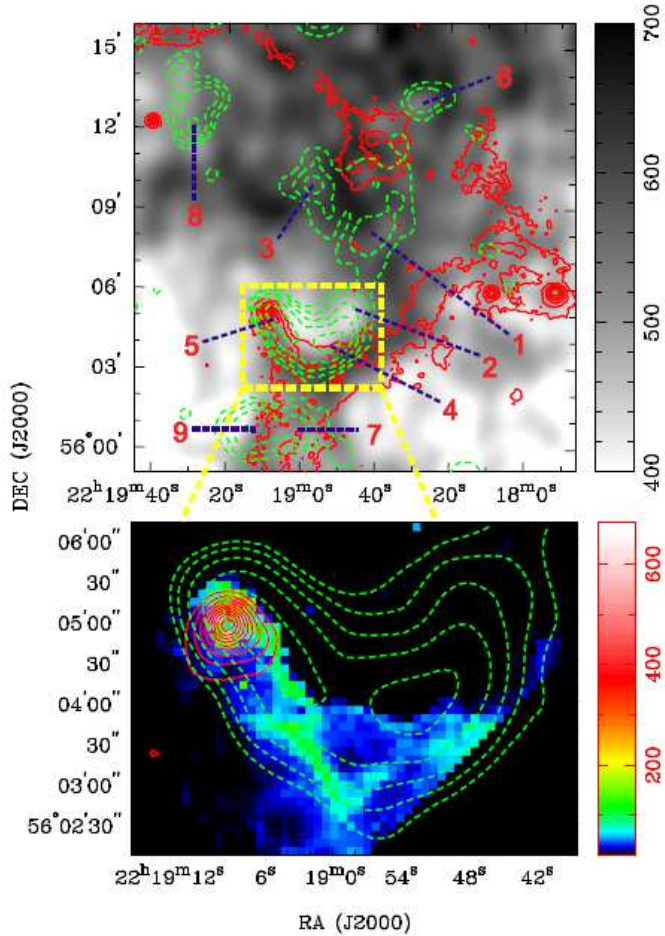


Fig. 10.— Upper: NVSS 1.4 GHz emission is shown in green dashed contours ($0.45 \text{ mJy } (1 \sigma) \times 3, 6, 9, \dots$), MSX A band emission in red solid contours (from 10% to 90%), and HI emission integrated from -48 km s^{-1} to -39 km s^{-1} in grey scale. Lower: NVSS 1.4 GHz emission is shown in green dashed contours, SCUBA $850 \mu\text{m}$ emission in red solid contours (from 10% to 90%) and IRAC $8 \mu\text{m}$ emission in color scale.

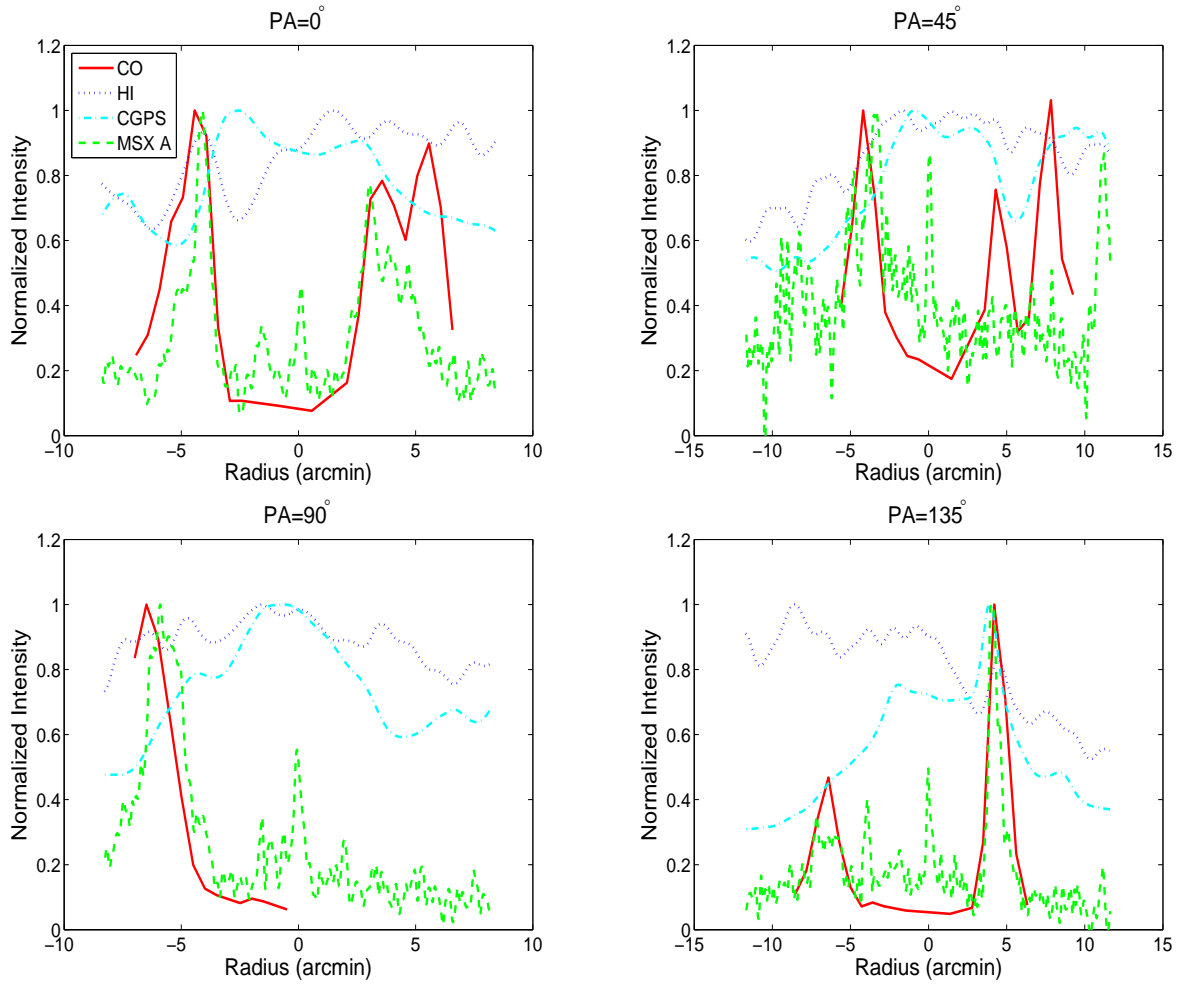
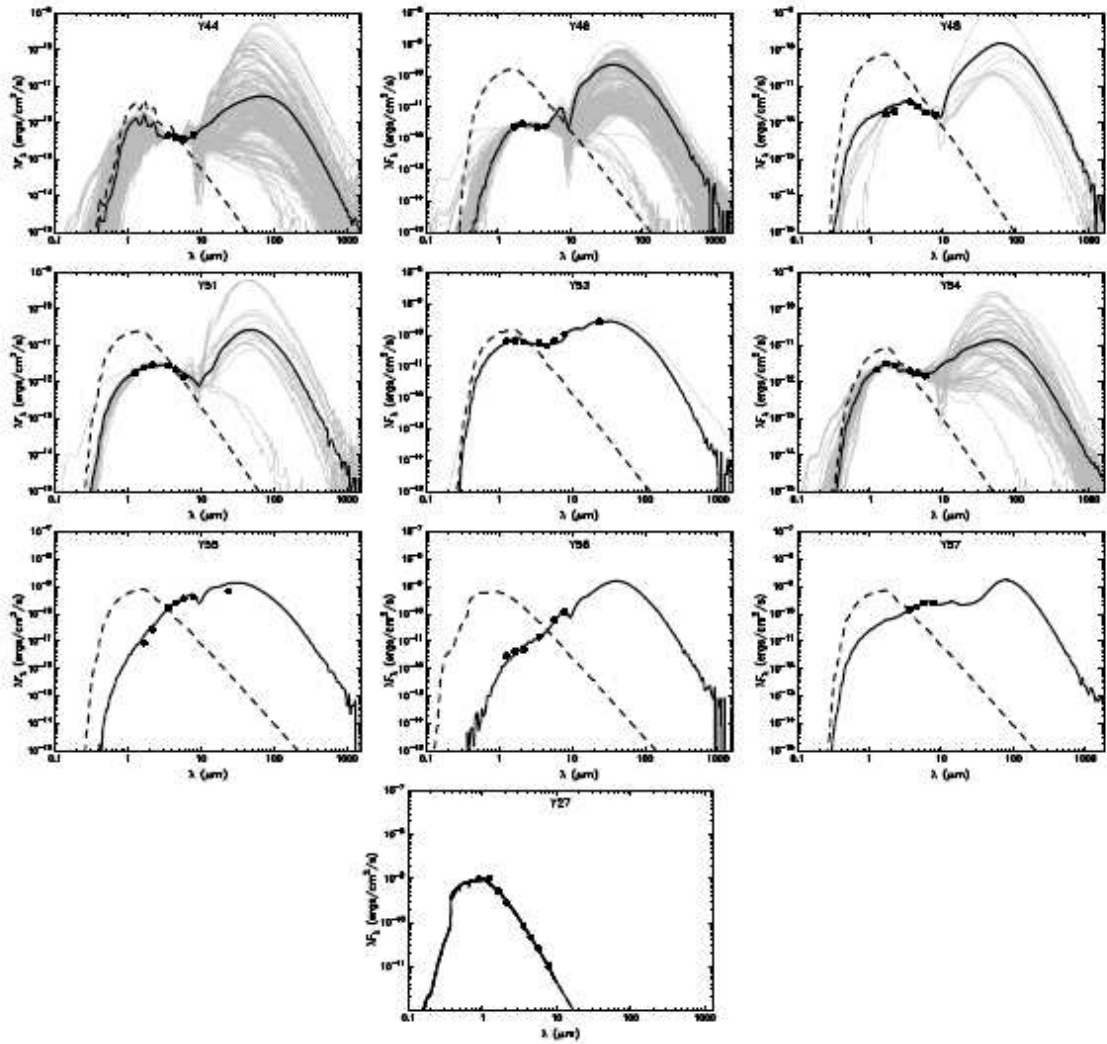


Fig. 11.— The normalized intensity distributions of CO, HI, 1420 MHz radio emission detected in CGPS and 8.3 μm emission detected in MSX A band along four orientations centered on the Wolf-Rayet star.



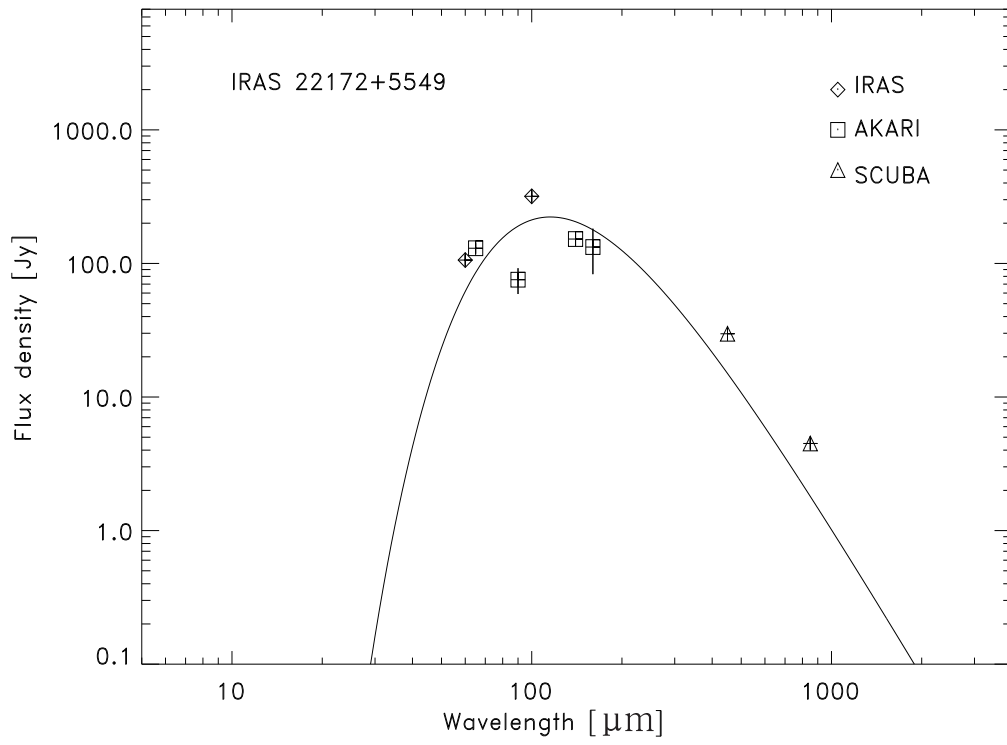


Fig. 13.— SED of molecular core A (IRAS 22172+5549). The solid curve represents the best fit.

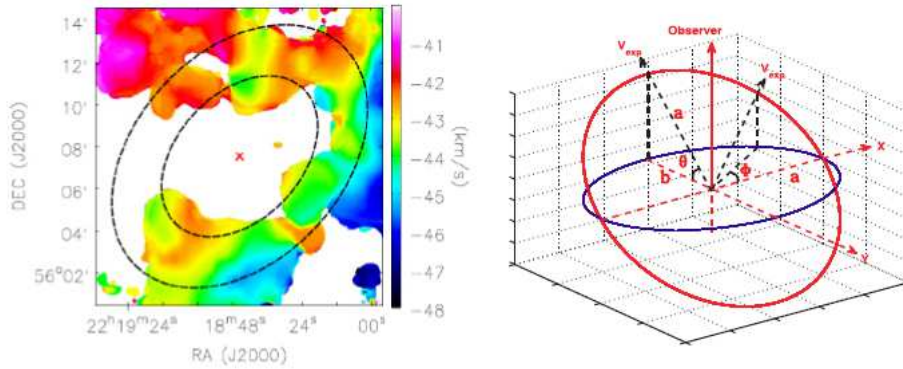


Fig. 14.— Left: First moment map of ^{12}CO (1-0). Two ellipses are drawn in for reference, to mark the boundaries of the interior and exterior of the molecular ring. Right: Coordinate system for describing the orientation in the sky of the ring nebular. The axis x and y lie on the plane of the sky. The WR star HD 211853 is located at the origin. The ring nebular is shown as red circle. The projection of the ring nebular in the sky plane is shown as blue ellipse. The lengths of the semimajor and semiminor axis of the ellipse are denoted as "a" and "b". The angle θ is the inclination angle between the plane of the ring nebular and the sky plane. The angle ϕ is the position angle measured from the major axis.

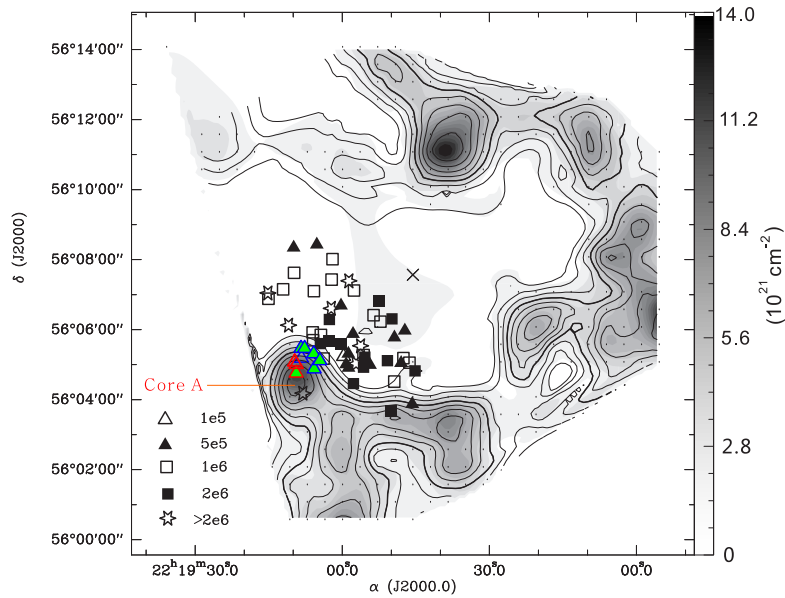


Fig. 15.— T_{ex} in contours overlaid on the column density of H_2 in grey scale. The contour levels are from 20% to 90% of the peak (24 K). The young stars in different age intervals are denoted as different markers on the plot as shown in the lower-left corner. The upper age of each interval is shown in the lower-left corner. The nine YSOs associated with core "A" are shown as color markers. The three most massive YSOs are shown as markers with red edges. The other six less massive ones are presented as markers with blue edges.

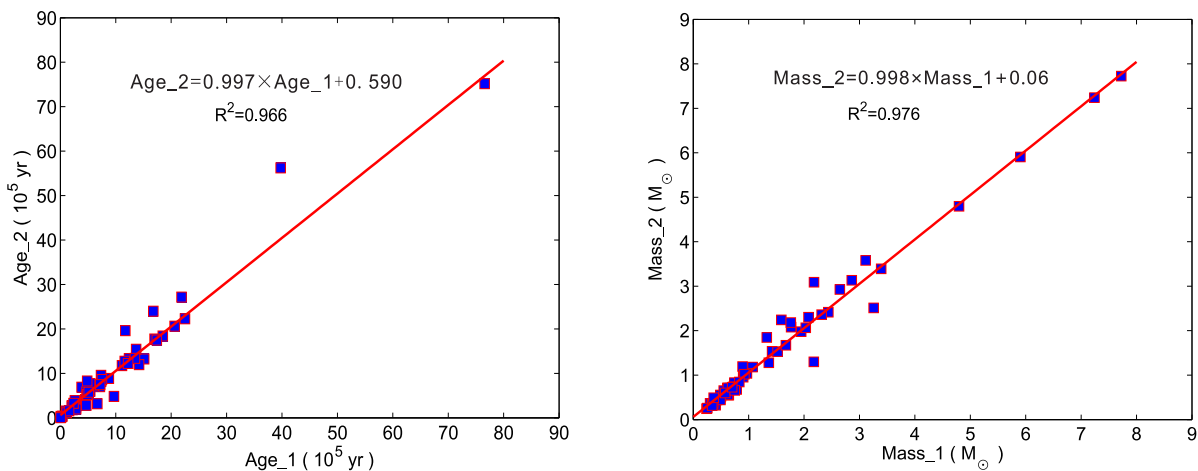


Fig. 16.— Comparison of the stellar mass and age of the YSOs in two runnings of the SED modeling. Left: Age comparison; Right: Mass comparison. The solid lines represent the linear fits. Age₁ and Mass₁ are the stellar age and mass obtained in the first running by exploring A_V in [2,2.5] mag. Age₂ and Mass₂ are the stellar age and mass obtained in the second running by exploring A_V in [0,2.5] mag.

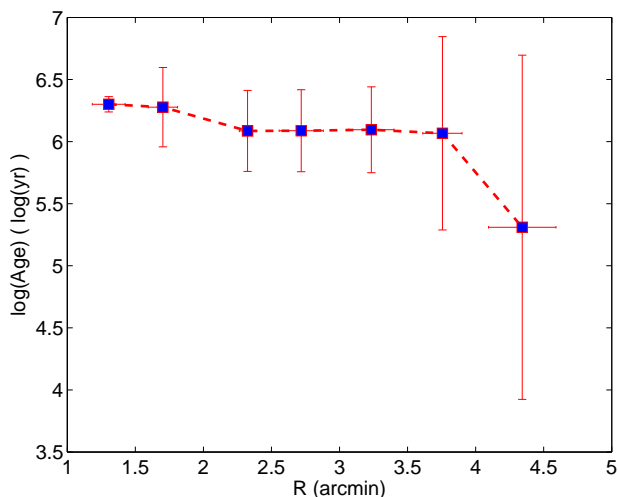


Fig. 17.— The distribution of 0.5' bin averaged ages of YSOs located between HD 211853 and core "A" as function of radii from the WR star. The errorbars represent the standard deviation in each bin.

Table 1. Observed parameters of ^{13}CO cores

Core	RA (J2000) (h m s)	DEC (J2000) ($^{\circ}$ ' ")	R ^a (pc)	V_{lsr} (km s ⁻¹)	$T_A(^{13}\text{CO})$ (K)	$\Delta V(^{13}\text{CO})$ (km s ⁻¹)	$T_A(^{12}\text{CO})$ (K)	$\Delta v(^{12}\text{CO})$ (km s ⁻¹)
A	22:19:09.4	56:04:46.5	1.0	-43.8(0.3)	2.6(0.1)	2.4(0.2)	9.2(0.3)	3.4(0.2)
B	22:18:38.4	56:03:25.4	1.4	-44.2(0.1)	2.2(0.1)	2.2(0.1)	7.5(0.1)	2.7(0.2)
C	22:18:20.1	56:06:00	0.9	-43.7(0.2)	1.2(0.1)	2.5(0.1)	8.5(0.2)	2.6(0.1)
D	22:18:03.1	56:08:07.6	1.0	-43.3(0.2)	2.5(0.1)	1.7(0.2)	7.6(0.3)	2.6(0.2)
E	22:18:03.1	56:05:42.7	0.8	-46.1(0.2)	1.8(0.2)	2.0(0.2)	7.9(0.2)	2.5(0.2)
F	22:18:08.8	56:11:17.3	1.1	-42.7(0.1)	2.1(0.2)	1.9(0.2)	7.7(0.3)	2.8(0.2)
G	22:18:39.1	56:11:17.3	1.3	-43.3(0.1)	2.9(0.1)	2.6(0.2)	10.1(0.2)	3.5(0.1)
H	22:19:26.6	56:11:17.3	0.5	-42.0(0.1)	1.0(0.1)	1.3(0.2)	3.7(0.2)	2.1(0.1)
I	22:18:17.6	56:12:23.4	1.0	-50.1(0.1)	1.4(0.1)	1.1(0.1)	4.9(0.1)	1.6(0.1)

^aTaking the distance as 3 kpc

Table 2. Derived parameters of ^{13}CO cores

Core	LTE					non-LTE										M_{vir}	M_J	M_{pv}	$P_{\text{ext}} / \text{k}$	$P_{\text{mol}} / \text{k}$
	$\tau(^{13}\text{CO})$	T_{ex}	N_{H_2}	n_{H_2}	M_{core}	T_{kin}	N_{H_2}	n_{H_2}	$T_{\text{ex}}(^{12}\text{CO})$	$\tau(^{12}\text{CO})$	$T_{\text{ex}}(^{13}\text{CO})$	$\tau(^{13}\text{CO})$	M_{core}							
	(K)	(10^{21} cm^{-2})	(10^3 cm^{-3})	(M_{\odot})	(K)	(10^{21} cm^{-2})	(10^3 cm^{-3})	(K)		(K)		(M_{\odot})	(M_{\odot})	(M_{\odot})	(M_{\odot})	($10^6 \text{ cm}^{-3}\text{K}$)	($10^5 \text{ cm}^{-3}\text{K}$)			
A	0.3	22	10.9	1.8	501	24.0(0.8)	9.0(0.4)	1.4(0.1)	21.7(0.5)	10.6(0.8)	15.6(0.5)	0.5	410(22)	504	544	199	5.8	5.1		
B	0.3	18.5	7.3	0.8	661	20.4(0.3)	7.8(0.3)	0.9	18.5(0.2)	15.6(0.7)	10.8(0.2)	0.9	701(30)	647	523	174	3.8	2.8		
C	0.2	20.5	5.2	0.9	193	26.5(1.1)	3.9(0.2)	0.7	20.5(0.4)	7.1(0.5)	9.9(0.4)	0.5	145(10)	473	870	703	0.6	2.8		
D	0.3	17.8	7.0	1.1	322	20.4(0.9)	6.9(0.3)	1.1(0.1)	18.6(0.5)	14.3(1.2)	12.2(0.3)	0.8	319(16)	357	232	150	0.6	2.1		
E	0.2	19	4.3	0.9	127	22.1(0.8)	5.0(0.5)	1.0(0.1)	19.3(0.4)	10.3(1.1)	11.6(0.6)	0.6	149(16)	336	383	288	0.6	2.6		
F	0.3	18.8	6.4	0.9	356	21.7(1.0)	6.1(0.6)	0.9(0.1)	18.9(0.5)	11.5(1.2)	11.1(0.5)	0.8	339(323)	439	350	235	0.6	2.1		
G	0.3	23.6	13.7	1.7	1061	26.2(0.6)	11.3(0.4)	1.4(0.1)	23.6(0.4)	11.2(0.6)	16.7(0.4)	0.6	877(36)	710	687	631	1.1	6.0		
H	0.3	11.2	1.8	0.6	21	11.7(0.6)	2.4(0.2)	0.8(0.1)	10.8(0.4)	15.8(1.9)	6.5(0.2)	0.9	27(3)	137	121	51	0.6	0.9		
I	0.3	13.2	2.2	0.3	99	14.6(0.3)	3.2(0.2)	0.5	13.2(0.2)	19.9(1.2)	7.0(0.2)	1.3	149(10)	231	103	27	0.6	0.4		

Table 3. Parameters of NVSS radio sources

Number	name	RA (J2000) (h m s)	DEC (J2000) ($^{\circ}$ ' ")	$S_{1.4}$ (mJy)	a (")	b (")	θ_R (')	n_e (cm^{-3})	EM (pc cm^{-6})	M_{HI} (M_{\odot})
1	221840+560824	22:18:40.77	+56:08:24.1	32.9 \pm 4.1	125.9	110.0	1.0	34	1322	1.6
2	221846+560534	22:18:46.86	+56:05:34.6	4.0 \pm 0.5	<80.5	<43.7	<0.5	<33	<633	<0.2
3	221856+560954	22:18:56.55	+56:09:54.6	20.3 \pm 2.5	83.7	65.7	0.6	54	2055	0.6
4	221852+560404	22:18:52.33	+56:04:04.0	103.4 \pm 4.1	103.0	56.1	0.6	117	9961	1.5
5	221905+560442	22:19:05.13	+56:04:42.5	87.6 \pm 3.4	98.6	29.3	0.4	181	16879	0.8
6	221826+561307	22:18:26.97	+56:13:07.7	10.0 \pm 1.4	71.7	<50.6	<0.5	<52	<1534	<0.3
7	221900+560045	22:19:00.72	+56:00:45.0	18.0 \pm 1.8	52.4	47.5	0.4	92	4026	0.3
8	221929+561202	22:19:29.67	+56:12:02.9	15.2 \pm 1.0	27.5	<31.8	<0.2	<185	<9675	<0.1
9	221912+560045	22:19:12.79	+56:00:45.0	38.2 \pm 2.7	83.2	64.5	0.6	75	3962	0.9

Table 4. The SED fitting results of the YSOs.

Name	RA (J2000) (h m s)	DEC (J2000) ($^{\circ}$ ' ")	Number	χ^2	log(d) log(kpc)	A_V (mag)	log(Age) log(yr)	M_* M_{\odot}	L_* L_{\odot}	log(\dot{M}_{env}) log($M_{\odot}\text{yr}^{-1}$)	log(\dot{M}_{env}) log($M_{\odot}\text{yr}^{-1}$)	log(\dot{M}_{disk}) log(M_{\odot})	log(\dot{M}_{disk}) log($M_{\odot}\text{yr}^{-1}$)	Stage
Y1	22:18:45.18	+56:04:49.3	35	20.8(1.5)	0.48	2.33(0.04)	6.07(0.08)	1.54(0.20)	8(2)	-1.36(0.42)	-5.72(0.35)	-1.90(0.11)	-7.13(0.11)	0/I
Y2	22:18:45.73	+56:03:52.6	100	12.3(1.0)	0.48(0.01)	2.29(0.06)	5.43(0.45)	1.18(0.26)	20(9)	-0.62(0.34)	-5.02(0.15)	-1.76(0.22)	-6.20(0.41)	0/I
Y3	22:18:46.31	+56:05:03.4	306	10.5(0.8)	0.47(0.01)	2.26(0.07)	5.88(0.24)	0.44(0.14)	1	-2.00(0.32)	-5.93(0.31)	-2.83(0.29)	-8.56(0.39)	0/I
Y4	22:18:47.26	+56:05:58.4	37	12.6(1.7)	0.47(0.01)	2.28(0.06)	5.40(0.10)	2.08(0.36)	37(18)	-0.56(0.26)	-4.71(0.34)	-1.95(0.27)	-6.68(0.31)	0/I
Y5	22:18:47.54	+56:05:11.2	107	8.0(1.1)	0.47(0.01)	2.27(0.08)	5.95(0.33)	0.24(0.07)	1	-1.26(0.62)	-5.48(0.37)	-2.52(0.20)	-7.64(0.42)	0/I
Y6	22:18:48.01	+56:05:02.9	1	58.1	0.46	2.00	5.18	1.98	31	-1.08	-4.74	-1.35	-6.75	0/I
Y7	22:18:49.37	+56:05:46.5	1	130.1	0.46	2.46	5.54	1.30	17	-1.11	-5.75	-1.20	-5.88	0/I
Y8	22:18:49.40	+56:04:31.0	1172	5.6(1.4)	0.47(0.01)	2.28(0.10)	5.86(0.42)	0.47(0.28)	4(7)	-0.61(1.36)	-4.94(1.00)	-2.36(0.54)	-7.25(0.97)	0/I
Y9	22:18:49.86	+56:06:18.5	879	14.3(0.6)	0.48(0.01)	2.25(0.06)	6.26(0.12)	1.04(0.16)	2(1)	-2.05(0.65)	-6.14(0.58)	-2.59(0.31)	-8.22(0.82)	III
Y10	22:18:50.13	+56:03:40.8	24	11.7(1.8)	0.47(0.01)	2.20(0.06)	6.29(0.18)	2.41(0.35)	28(8)	-0.73(0.28)	-4.99(0.24)	-1.49(0.17)	-6.69(0.31)	0/I
Y11	22:18:50.78	+56:05:06.8	835	5.1(1.4)	0.48(0.01)	2.26(0.10)	6.12(0.29)	0.52(0.19)	1(1)	-1.77(0.60)	-5.79(0.54)	-2.66(0.33)	-8.01(0.64)	0/I
Y12	22:18:52.22	+56:06:13.7	306	7.4(1.1)	0.48(0.01)	2.25(0.08)	5.78(0.40)	0.55(0.25)	4(4)	-1.09(0.50)	-5.24(0.35)	-2.42(0.24)	-7.64(0.25)	0/I
Y13	22:18:52.49	+56:06:48.8	550	12.3(1.1)	0.48(0.01)	2.28(0.06)	6.06(0.16)	0.71(0.15)	2(3)	-1.34(1.35)	-5.43(1.83)	-2.37(0.28)	-7.86(1.87)	0/I
Y14 ^a	22:18:52.69	+56:06:05.1	1	30154.2	0.51	2.00	6.09	3.39	36	-2.98	-8.68	-2.20	-7.59	III
Y15	22:18:53.62	+56:06:24.8	465	15.0(1.2)	0.48(0.01)	2.34(0.05)	5.92(0.14)	0.64(0.12)	2	-1.46(0.58)	-5.63(0.42)	-2.33(0.20)	-8.14(0.24)	0/I
Y16	22:18:54.35	+56:04:59.6	81	6.9(1.3)	0.48(0.01)	2.29(0.08)	5.26(0.70)	0.42(0.14)	4(2)	-0.70(0.24)	-4.96(0.20)	-2.14(0.29)	-6.00(0.47)	0/I
Y17	22:18:55.39	+56:05:12.9	259	5.1(1.5)	0.48(0.01)	2.26(0.10)	6.12(0.30)	0.95(0.30)	3(2)	-1.06(0.78)	-5.30(0.57)	-2.40(0.30)	-7.81(0.36)	0/I
Y18	22:18:55.67	+56:05:16.3	44	7.6(1.3)	0.47(0.01)	2.22(0.07)	6.08(0.24)	1.53(0.42)	11(7)	-0.55(0.44)	-4.91(0.39)	-2.07(0.19)	-7.37(0.30)	0/I
Y19	22:18:55.67	+56:04:55.4	2584	1.7(1.9)	0.47(0.02)	2.22(0.16)	5.98(0.57)	0.36(0.28)	1(1)	-1.89(2.11)	-5.87(0.83)	-2.91(0.89)	-8.45(4.77)	0/I
Y20 ^a	22:18:56.14	+56:05:48.6	1	2131.5	0.48	2.00(0.01)	5.61	4.42	63	-1.10	-5.32	-2.86	-9.64	0/I
Y21	22:18:56.27	+56:05:32.3	894	7.1(1.2)	0.48(0.01)	2.27(0.08)	6.19(0.23)	0.83(0.25)	2(1)	-1.43(0.59)	-5.56(0.48)	-2.46(0.31)	-8.06(0.39)	0/I
Y22	22:18:57.18	+56:05:02.0	1	162.5	0.48	2.00	6.38	3.13	128	-2.63		-7.27	-13.27	III
Y23	22:18:57.62	+56:07:07.0	43	46.7(0.8)	0.48	2.32(0.03)	5.84(0.08)	1.19(0.10)	6(1)	-1.22(0.14)	-5.34(0.20)	-1.99(0.10)	-7.54(0.09)	0/I

Table 4—Continued

Name	RA (J2000)	DEC (J2000)	Number	χ^2	log(d)	A_v	log(Age)	M_*	L_*	log(\dot{M}_{env})	log(\dot{M}_{env})	log(\dot{M}_{disk})	log(\dot{M}_{disk})	Stage
	(h m s)	($^{\circ}$ ' ")			log(kpc)	(mag)	log(yr)	M_{\odot}	L_{\odot}	log(M_{\odot})	log($M_{\odot}\text{yr}^{-1}$)	log(M_{\odot})	log($M_{\odot}\text{yr}^{-1}$)	
Y24	22:18:57.71	+56:04:27.5	1084	4.5(1.7)	0.48(0.01)	2.28(0.10)	6.11(0.35)	0.45(0.24)	2(5)	-1.05(2.14)	-5.28(1.84)	-2.50(0.36)	-7.52(1.26)	0/I
Y25	22:18:57.82	+56:05:52.6	270	16.0(0.8)	0.47(0.01)	2.27(0.06)	5.34(0.47)	0.44(0.18)	5(5)	-0.42(0.65)	-4.90(0.50)	-2.29(0.39)	-6.84(1.40)	0/I
Y26	22:18:58.38	+56:04:23.3	24	15.1(1.4)	0.48	2.34(0.06)	6.88(0.04)	2.24(0.28)	46(29)	0.16(0.39)	-6.38(0.39)	-2.21(0.25)	-7.46(0.37)	III
Y27 ^b	22:18:58.68	+56:07:23.6	1	19476.0	0.51	2.50	6.11	14.60	19200	-7.86		-8.04	-9.44	III
Y28	22:18:58.71	+56:04:54.5	53	5.3(1.6)	0.48(0.01)	2.24(0.09)	5.50(0.76)	0.55(0.39)	6(8)	-0.55(0.95)	-4.99(0.75)	-2.41(0.67)	-7.32(0.35)	0/I
Y29	22:18:58.76	+56:05:18.8	1106	4.6(1.6)	0.47(0.01)	2.26(0.10)	5.55(0.38)	0.26(0.15)	1(1)	-1.61(0.67)	-5.60(0.62)	-2.85(0.42)	-8.17(1.60)	0/I
Y30	22:18:59.21	+56:05:00.6	62	2.9(2.1)	0.47(0.01)	2.27(0.10)	5.46(0.77)	0.56(0.25)	3(4)	-1.07(0.43)	-5.23(0.51)	-2.19(0.34)	-7.95(0.56)	0/I
Y31	22:18:59.72	+56:05:13.9	1	128.7	0.49	2.02	4.58	1.67	33	-0.33	-4.82	-1.24	-6.01	0/I
Y32	22:19:00.08	+56:03:14.8	314	18.4(0.7)	0.48(0.01)	2.31(0.04)	6.88(0.02)	2.36(0.06)	31(3)	-3.63(0.21)		-3.06(0.29)	-7.99(0.52)	III
Y33	22:19:00.18	+56:05:34.7	55	6.0(1.5)	0.47(0.01)	2.22(0.08)	6.01(0.36)	0.32(0.11)	2(1)	-1.17(0.39)	-5.29(0.40)	-2.35(0.21)	-7.26(0.43)	0/I
Y34	22:19:00.26	+56:06:41.4	178	4.4(1.6)	0.48(0.01)	2.22(0.09)	5.59(0.57)	0.71(0.35)	6(8)	-0.72(0.60)	-5.03(0.42)	-2.36(0.35)	-7.50(0.56)	0/I
Y35	22:19:02.01	+56:07:08.5	7	22.0(1.2)	0.47	2.15(0.04)	6.43(0.09)	2.30(0.11)	12(2)	-1.65(0.23)	-5.96(0.24)	-1.85(0.19)	-7.75(0.24)	0/I
Y36	22:19:02.01	+56:08:00.7	1391	7.8(1.1)	0.48(0.01)	2.27(0.08)	5.85(0.33)	0.34(0.16)	1(2)	-1.32(1.17)	-5.48(1.20)	-2.64(0.34)	-7.68(1.05)	0/I
Y37	22:19:02.18	+56:07:25.8	1174	3.7(1.7)	0.48(0.01)	2.28(0.11)	5.98(0.41)	0.65(0.33)	2(2)	-1.25(0.74)	-5.41(0.61)	-2.44(0.37)	-7.78(0.39)	0/I
Y38	22:19:02.26	+56:06:36.5	320	3.7(1.7)	0.48(0.01)	2.28(0.10)	6.25(0.26)	1.02(0.34)	3(2)	-1.25(1.46)	-5.58(0.97)	-2.41(0.46)	-8.06(0.43)	0/I
Y39	22:19:02.62	+56:06:17.3	706	4.2(1.7)	0.47(0.01)	2.26(0.11)	6.13(0.33)	0.44(0.25)	2(5)	-1.05(2.41)	-5.23(2.22)	-2.61(0.42)	-7.79(1.71)	0/I
Y40	22:19:02.77	+56:05:40.6	116	14.9(1.2)	0.48(0.01)	5.03(0.53)	6.27(0.12)	1.85(0.27)	20(10)	-1.25(0.60)	-5.66(0.48)	-2.27(0.18)	-8.16(0.31)	0/I
Y41	22:19:03.80	+56:05:10.3	81	12.1(1.2)	0.47(0.01)	2.27(0.06)	5.85(0.36)	0.68(0.22)	4(2)	-1.04(0.46)	-5.26(0.28)	-2.07(0.13)	-7.21(0.24)	0/I
Y42	22:19:04.36	+56:05:50.8	395	7.1(1.2)	0.48(0.01)	2.29(0.08)	5.94(0.41)	0.74(0.36)	11(12)	0.00(0.86)	-4.59(0.56)	-2.04(0.48)	-6.49(0.77)	0/I
Y43	22:19:04.46	+56:05:36.0	1	113.3	0.48	2.42	6.09	3.39	36	-2.98	-8.68	-2.20	-7.59	III
Y44	22:19:04.50	+56:05:07.8	215	6.3(1.4)	0.47(0.01)	2.26(0.09)	5.62(0.52)	0.68(0.34)	10(10)	-0.32(0.70)	-4.72(0.58)	-2.19(0.43)	-6.68(1.48)	0/I
Y45	22:19:05.21	+56:08:25.8	10	46.4(0.9)	0.49	2.31(0.03)	5.42(0.04)	0.85(0.08)	7(1)	-0.66(0.14)	-4.92(0.14)	-2.01(0.07)	-7.22(0.08)	0/I
Y46	22:19:05.72	+56:04:52.7	218	6.7(1.3)	0.48(0.01)	2.27(0.09)	5.30(0.59)	2.07(0.69)	62(37)	0.18(0.60)	-4.60(0.26)	-1.42(0.37)	-6.17(0.36)	0/I

Table 4—Continued

Name	RA (J2000) (h m s)	DEC (J2000) (° ′ ″)	Number	χ^2	log(d) log(kpc)	A_v (mag)	log(Age) log(yr)	M_* M_\odot	L_* L_\odot	log(M_{env}) log(M_\odot)	log(\dot{M}_{env}) log($M_\odot \text{yr}^{-1}$)	log(M_{disk}) log(M_\odot)	log(\dot{M}_{disk}) log($M_\odot \text{yr}^{-1}$)	Stage
Y47	22:19:05.79	+56:07:05.9	138	10.9(0.9)	0.48(0.01)	2.29(0.06)	5.87(0.12)	0.68(0.15)	2	-1.87(0.62)	-6.15(0.31)	-2.58(0.22)	-8.21(0.31)	III
Y48	22:19:05.82	+56:05:18.8	10	108.1(0.6)	0.47	2.29(0.02)	5.06(0.03)	2.51(0.19)	74(13)	0.72(0.06)	-4.08(0.04)	-2.22(0.04)	-7.37(0.08)	0/I
Y49	22:19:05.94	+56:05:41.7	262	4.9(1.6)	0.48(0.01)	2.27(0.09)	5.89(0.31)	0.71(0.31)	5(8)	-0.74(0.95)	-4.83(1.21)	-2.45(0.75)	-7.32(2.15)	0/I
Y50	22:19:06.02	+56:05:55.3	1	41.0	0.51	2.00	5.77	3.58	24	-1.46	-5.25	-5.07	-10.84	0/I
Y51	22:19:07.65	+56:05:28.6	22	14.5(1.6)	0.48(0.01)	2.23(0.06)	5.68(0.30)	3.09(0.40)	67(25)	-0.42(0.13)	-4.60(0.15)	-1.61(0.27)	-6.47(0.42)	0/I
Y52	22:19:08.03	+56:04:11.1	1	130.6	0.44	2.00	6.31	4.80	408	-5.15		-0.82	-7.62	III
Y53	22:19:08.30	+56:05:11.0	2	387.4(0.6)	0.45	2.16(0.01)	4.51(0.02)	2.93(0.03)	98(1)	0.07(0.01)	-4.41(0.01)	-1.14(0.03)	-5.57(0.03)	0/I
Y54	22:19:08.45	+56:05:28.7	72	9.4(1.8)	0.48(0.01)	2.27(0.07)	5.51(0.35)	1.28(0.43)	18(10)	0.27(0.49)	-4.42(0.27)	-1.61(0.18)	-6.42(0.17)	0/I
Y55	22:19:09.38	+56:05:00.4	1	299.6	0.46	2.50	4.12	7.72	607	1.19	-4.40	-0.92	-5.96	0/I
Y56	22:19:09.39	+56:04:45.7	1	193.3	0.44	2.00	5.20	7.24	1003	1.88	-4.04	-0.96	-7.04	0/I
Y57	22:19:09.70	+56:05:04.8	1	30.7	0.48	2.00	3.61	5.91	478	1.22	-2.92	-2.32	-6.35	0/I
Y58	22:19:09.84	+56:07:37.4	1438	4.1(1.5)	0.48(0.01)	2.27(0.11)	5.72(0.54)	0.36(0.24)	2(3)	-1.33(0.92)	-5.42(0.53)	-2.55(0.43)	-7.76(0.88)	0/I
Y59	22:19:09.94	+56:08:20.5	174	8.4(1.1)	0.48(0.01)	2.27(0.07)	5.45(0.40)	0.32(0.14)	2(2)	-1.19(0.36)	-5.28(0.25)	-2.42(0.28)	-7.33(0.52)	0/I
Y60	22:19:10.94	+56:06:07.6	1134	5.4(1.4)	0.48(0.01)	2.26(0.09)	6.24(0.23)	0.60(0.20)	1	-1.97(0.99)	-6.00(0.68)	-2.77(0.48)	-8.48(0.47)	III
Y61	22:19:12.07	+56:07:09.1	54	9.8(1.2)	0.47(0.01)	2.20(0.07)	5.76(0.18)	0.66(0.14)	3(2)	-1.12(0.36)	-5.31(0.25)	-2.28(0.37)	-7.15(0.45)	0/I
Y62	22:19:13.80	+56:07:48.4	305	15.9(1.2)	0.49(0.01)	2.82(0.42)	6.75(0.04)	2.18(0.12)	26(7)	-3.39(0.40)	-8.72(2.28)	-3.04(0.82)	-10.24(0.57)	III
Y63	22:19:15.06	+56:06:53.0	194	4.0(1.7)	0.48(0.01)	2.24(0.10)	5.92(0.47)	0.49(0.24)	1(1)	-1.62(0.89)	-5.73(0.75)	-2.49(0.48)	-8.20(0.44)	0/I
Y64	22:19:15.18	+56:07:02.8	2239	2.2(1.7)	0.47(0.02)	2.26(0.14)	6.35(0.29)	0.73(0.35)	1(2)	-1.85(13.16)	-6.11(9.52)	-2.85(0.85)	-8.51(5.91)	III

^aBad fit.^bEvolved star?